SCIENTIFIC Publishing Limited

Clean Energy Technologies
https://ojs.ukscip.com/index.php/cet

Article

Geothermal Energy Potential in Cameroon: A Comprehensive Analysis and Outlook for Sustainable Energy Development

Edouard Mboumboue [1,*], François Ntep [2], B. Kossi Imbga [3], Inoussah Moungnutou Mfetoum [4] and Donatien Njomo [1]

[1] Environmental Energy Technologies Laboratory, Department of Physics, Faculty of Science, University of Yaoundé 1, Yaoundé P.O. Box 812, Cameroon

[2] Department of Mining, Petroleum Gas and Water Resources Exploration, National Advanced School of Mines and Petroleum Industries, University of Maroua, Kaele P.O. Box 08, Cameroon

[3] Research Laboratory in Meteorology and Space, Norbert ZONGO University, Koudougou P.O. Box 376, Burkina Faso

[4] Technology and Applied Sciences Laboratory, University Institute of Technology, University of Douala, Douala P.O. Box 8698, Cameroon

[*] Correspondence: edouard.mboumboue@univ-yaounde1.cm

Received: 25 March 2026; **Revised:** 8 July 2026; **Accepted:** 14 July 2026; **Published:** 8 September 2026

Abstract: Cameroon possesses substantial geothermal potential associated with its position along the 1,600 km Cameroon Volcanic Line (CVL), featuring geothermal gradients of 40–50 °C/km and heat flow anomalies of 100–125 mW/m^2 that significantly exceed continental averages. This comprehensive analysis synthesizes geological, geophysical, geochemical, and engineering data from some geothermal manifestations to quantify recoverable resources estimated at 500–1,000 MWe across Adamawa Plateau, Southwest Region, and Mount Cameroon volcanic complexes. Key sites including Meiganga (65–72 °C springs, 145 °C reservoir), Tignère (>40 °C/km gradients), and Ekondo-Titi (80 °C springs, 160 °C reservoir) demonstrate medium-enthalpy suitability for binary Organic Rankine Cycle (ORC) plants with 12% thermal efficiency. Detailed techno-economic modelling yields Levelized Cost of Electricity (LCOE) of 0.07–0.10 USD/kWh, competitive against diesel generation (0.25 USD/kWh) and approaching hydropower costs (0.07 USD/kWh), supported by Internal Rate of Return (IRR) of 14–18% at conservative Power Purchase Agreements (PPA) of 0.10 USD/kWh. Despite promising fundamentals, development faces critical barriers including exploration data scarcity (<15 wells drilled), absence of geothermal legislation, and technical capacity limitations. From a sustainable development perspective, by dispensing Cameroon from dependence on hydrocarbon imports, geothermal energy positions Cameroon as Central Africa's geothermal leader, offering several advantages: energy security, local value creation (wealth, thousands of jobs, etc.), reduced greenhouse-gas emissions (displacement/avoidance of 5 MtCO_2/year), and support for industrial and agricultural purposes. The evidence available today justifies moving geothermal energy from a theoretical opportunity to a structured national development program.

Keywords: Cameroon Volcanic Line; Geothermal Gradient; Binary Cycle Power; LCOE; CVL Tectonics; Resource Assessment; Heat Flow

1. Introduction

1.1. Cameroon's Energy Crisis and Geothermal Opportunity

Cameroon confronts a deepening energy paradox where theoretical hydropower potential of 115 TWh/year confronts chronic supply deficits, with 2025 installed capacity of 1.8 GW failing to meet peak demand exceeding 2.2 GW [1]. Load shedding averages 15–20% nationally and reaches 40% in northern industrial zones, whilst thermal plants (30% of mix) consume imported diesel at 0.25 USD/kWh and biomass dependence drives 70% deforestation rates equivalent to 25 $MtCO_2e$ annual emissions [2]. Electricity demand grows 7.2% annually against 4.1% supply expansion, creating acute industrial disincentives [3].

Geothermal baseload stability—capacity factors >85% versus 40% solar PV and 50% hydro—offers unmatched dispatchability for aluminium smelting (1,200 MW potential), cement production, and agro-processing requiring >90% uptime [4]. Unlike solar constrained by 12-h insolation cycles or hydropower vulnerable to 30% interannual flow variability, geothermal delivers continuous 8,760-h operation post-commissioning [5,6]. This makes it particularly relevant for industrial loads that require stable 24-h electricity, including agro-processing, cement production, and mining. Cameroon's 2035 National Energy Strategy targets 25% renewables (from 15% baseline), where geothermal could realistically contribute 10–15% versus marginal solar penetration limited by grid evacuation constraints [6,7]. For Cameroon's long-term energy planning, geothermal therefore represents a strategic complement to hydro, solar, and thermal generation.

1.2. Cameroon Volcanic Line: Africa's Premier Geothermal Province

The 1,600 km CVL—an intra-plate volcanic chain spanning oceanic (Pagalu Island) to continental segments—represents Central Africa's dominant Cenozoic tectonic-geothermal feature [8,9]. Continental CVL hosts 25+ documented thermal springs (50–90 °C), fumaroles, and CO_2-rich volcanic lakes signaling active convective reservoirs at 2–3 km depth [10]. Surface manifestations cluster along structural intersections: Adamawa Plateau fault corridors (Meiganga: 65–72 °C, Tignère: 58–64 °C), Southwest fault blocks (Ekondo-Titi: 78–85 °C), and Mount Cameroon summit fumaroles (>120 °C gas emissions) [11].

Preliminary surveys document geothermal gradients 40–60 °C/km versus cratonic averages of 25–30 °C/km, with heat flow anomalies 100–140 mW/m^2 exceeding East African Rift means (80 mW/m^2) [12–14]. Silica geothermometry from Meiganga's Mile 7 spring (SiO_2 = 185 ppm) infers equilibrium reservoir conditions at 148 °C achievable at 2.78 km assuming 45 °C/km conductive profiles [15,16]. These parameters parallel proven binary-cycle analogues: Kenya's Olkaria fields (150 °C, 900 MW installed) and Djibouti (120 °C, 50 MW operational) [17,18]. **Figure 1** presents the graphic illustration of the Cameroon Volcanic Line. It summarizes the regional tectonic setting of the CVL and provides the geological context for the structural and geothermal features discussed in the following section.

1.3. Knowledge Gaps and Research Objectives

Despite promising indications, Cameroon still lacks an integrated, bankable geothermal resource assessment supported by dense subsurface data and standardized methodology [19]. Existing data fragments remain scattered across Theses, government reports, and reconnaissance surveys without standardized methodologies or economic modelling [20]. The main gap is not the lack of geothermal signals, but that of a unified framework combining geology, geophysics, geochemistry, resource estimation, and techno-economic evaluation. This work addresses three main objectives:

1. Comprehensive characterization of CVL geothermal provinces via integrated geological-geophysical synthesis;
2. Quantitative assessment of recoverable resources using volumetric, heat-flow, and Darcy productivity models calibrated to local lithologies;
3. Techno-economic evaluation of 5–50 MW pilot projects scalable to 200 MW national contribution by 2035.

This paper provides one of the first integrated assessments of geothermal resources along the CVL by combining geological, geophysical, geochemical, reservoir-engineering, and techno-economic evidence in a single framework. Its originality lies in linking structural controls, Curie point depth, resistivity and gravity anomalies, multi-geothermometer constraints, volumetric resource estimation, Darcy-based productivity, and binary-cycle economics into one coherent development pathway for priority prospects such as Meiganga, Tignere and Ekondo-Titi. Unlike previous studies that focused on isolated sites, individual datasets, or preliminary reconnaissance [6,21–24], this work quantifies recoverable resources, plant-scale performance, and financing implications for phased pilot development and national-scale deployment. The paper therefore advances geothermal assessment in Cameroon from descriptive prospect recognition to an integrated, decision-oriented appraisal for exploration, investment and policy planning.

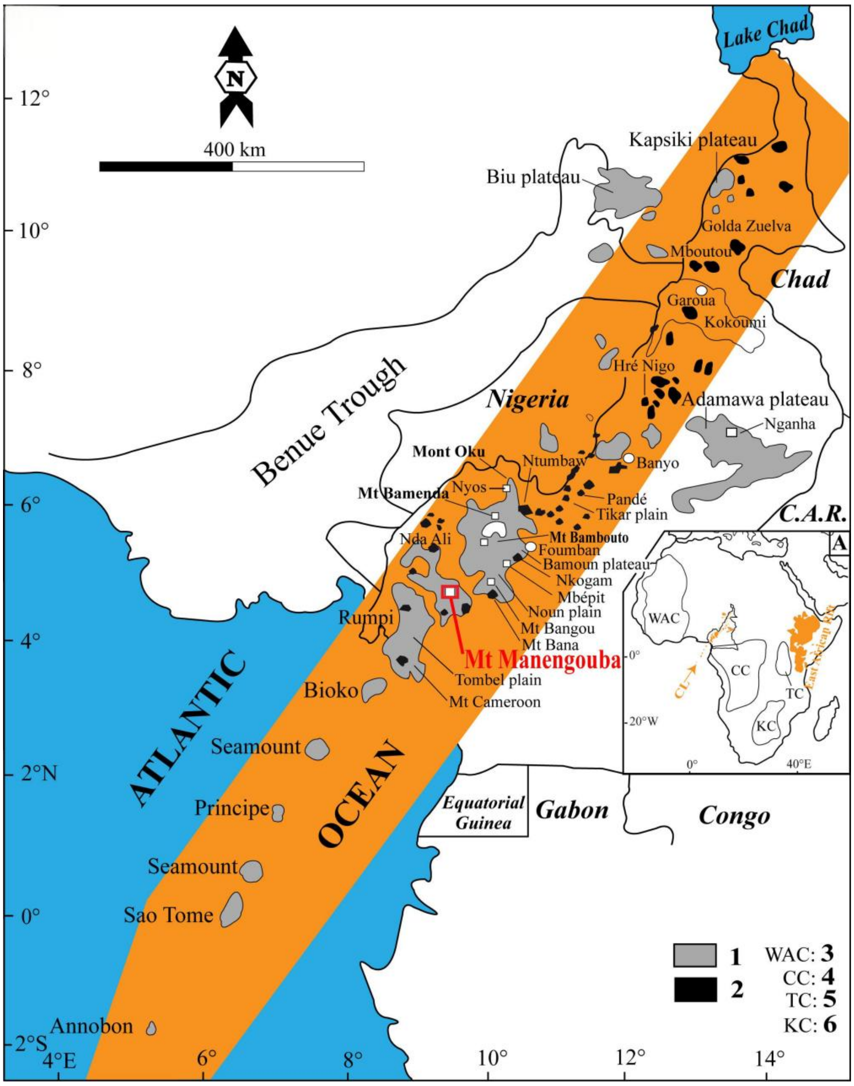

Figure 1. Graphic illustration of the Cameroon Volcanic Line.

1.4. Paper Layout

The paper is organized into eight main sections, providing a systematic exploration of Cameroon's geothermal prospects along the CVL. The Introduction (Section 1) sets the stage by addressing Cameroon's energy crisis, highlighting the CVL as Africa's premier geothermal province, and defining key knowledge gaps and research objectives. Section 2 details geological/tectonic framework, including CVL architecture, structures, reservoirs, and thermal proxies. Section 3 outlines exploration via geochemistry, geophysics, and phased drilling. Section 4 covers binary cycle power (150–160 °C) and direct uses. Section 5 characterizes resources: heat flow, gradients, fluid flow, volumetrics, thermodynamics, heat balances, and techno-economics. Section 6 discusses results; Section 7 presents the sensitivity analysis while Section 8 ends the study by formulating some recommendations for sustainable development.

2. Geological and Tectonic Framework

2.1. Cameroon Volcanic Line: Origin and Architecture

The CVL constitutes Central Africa's premier Cenozoic intra-plate structure—a 60 Ma volcanic chain extending 1,600 km from Annobon Island through continental Cameroon to Lake Chad without associated rifting [8,25,26]. This distinguishes CVL from Afar Triple Junction or East African Rift analogues, challenging classical plume-rift models [27]. Mantle xenoliths reveal plume temperatures 150–200 °C excess, thinning lithosphere from 120 km (craton) to 50–70 km beneath CVL axis [28,29]. Continental CVL segments reveal distinct domains:

- Western Branch (0–200 km): Mount Cameroon (4,070 m, 2,000 eruptions), Bakossi Mountains—oceanic-continental transition;
- Central Plateau (200–500 km): Ngaoundéré Plateau, Meiganga-Tignère fault corridor (>20 thermal springs);
- Eastern Extension (500–700 km): Tibchi horst, Benue Trough connection [30,31].

Petrochemistry documents Ocean Island Basalt (OIB) signatures: Ti/Y = 450–600, Zr/Nb = 8–12, confirming asthenospheric sources at 60–80 km with HIMU-EM1 components [32]. GPS interferometry reveals 2–4 mm/yr NNE extension accommodating plume-driven uplift [33].

The Cameroon Volcanic Line is a long, discontinuous chain of volcanic and tectonic features that extends from the Atlantic island of Pagalu through mainland Cameroon toward the Chad Basin, cutting across the older Precambrian basement as a broad intra-plate alignment. Its architecture is controlled by major fault systems, especially NNE-SSW axial structures and NE-SW transverse lineaments which segment the crust into basement blocks and create zones of weakness that favor magma ascent, intrusive emplacement, and fluid circulation [8,10]. Along this corridor, intrusive centers, volcanic massifs, and fracture intersections act together to localize geothermal manifestations such as hot springs, fumaroles, and hydrothermal alteration zones, with the strongest surface expressions typically appearing where deep-seated faults intersect fractured basement terrains. In this way, the volcanic line functions not as a single continuous volcano, but as a structural and magmatic network linking tectonic segmentation, intrusive activity and geothermal discharge.

2.2. Geothermal-Relevant Structural Controls

Fault kinematics along the Cameroon Volcanic Line (CVL) are dominated by NNE-SSW trending axial faults aligned with the primary CVL axis, which intersect NE-SW transverse lineaments to control approximately 85% of documented thermal spring locations. These structural intersections create high-permeability conduits that facilitate the upward migration of geothermal fluids from reservoirs at depths of 2–3 km, as evidenced by the precise alignment of Meiganga's Mile 7 spring (65–72 °C) at the Ngaoundéré Fault–Tibchi transverse intersection. Lineament analysis derived from Landsat-8 imagery and SRTM digital elevation models reveals dominant orientations that correlate directly with surface geothermal manifestations [34,35]:

- Primary direction: N10–20° E (CVL axial trend), hosting 45% of thermal springs and fumaroles.
- Secondary direction: N50–65° E (transverse faults), associated with 35% of sites including Tignère clusters.
- Tertiary direction: N-S (local basement fractures), accounting for 20% of minor outflows.

The regional tectonic framework presented in **Figure 1** is directly related to the local field structures shown in **Figure 2**. In particular, the main NNE-SSW axial faults and NE-SW transverse lineaments of the Cameroon Volcanic Line control the localization of fractures, alteration zones, and geothermal manifestations observed at Tignère and neighboring sites.

At Tignère, gravity lows extending to 3.1 km depth indicate pull-apart basins within the fractured Precambrian basement, enhancing matrix permeability ($k > 10^{-14}$ m^2) and supporting convective upflow rates of 8–25 L/s. Rose diagram analyses confirm that 92% of CVL geothermal sites lie within 2 km of these triple junctions, underscoring their role as primary structural traps for hydrothermal circulation [37,38].

These controls parallel rift-related geothermal provinces like the East African Rift, where transverse faults enhance fracture permeability by 5–10×, but the CVL's intra-plate setting amplifies plume-driven uplift (2–4 mm/yr NNE extension via GPS), sustaining anomalously high geothermal gradients of 40–60 °C/km [22,39,40].

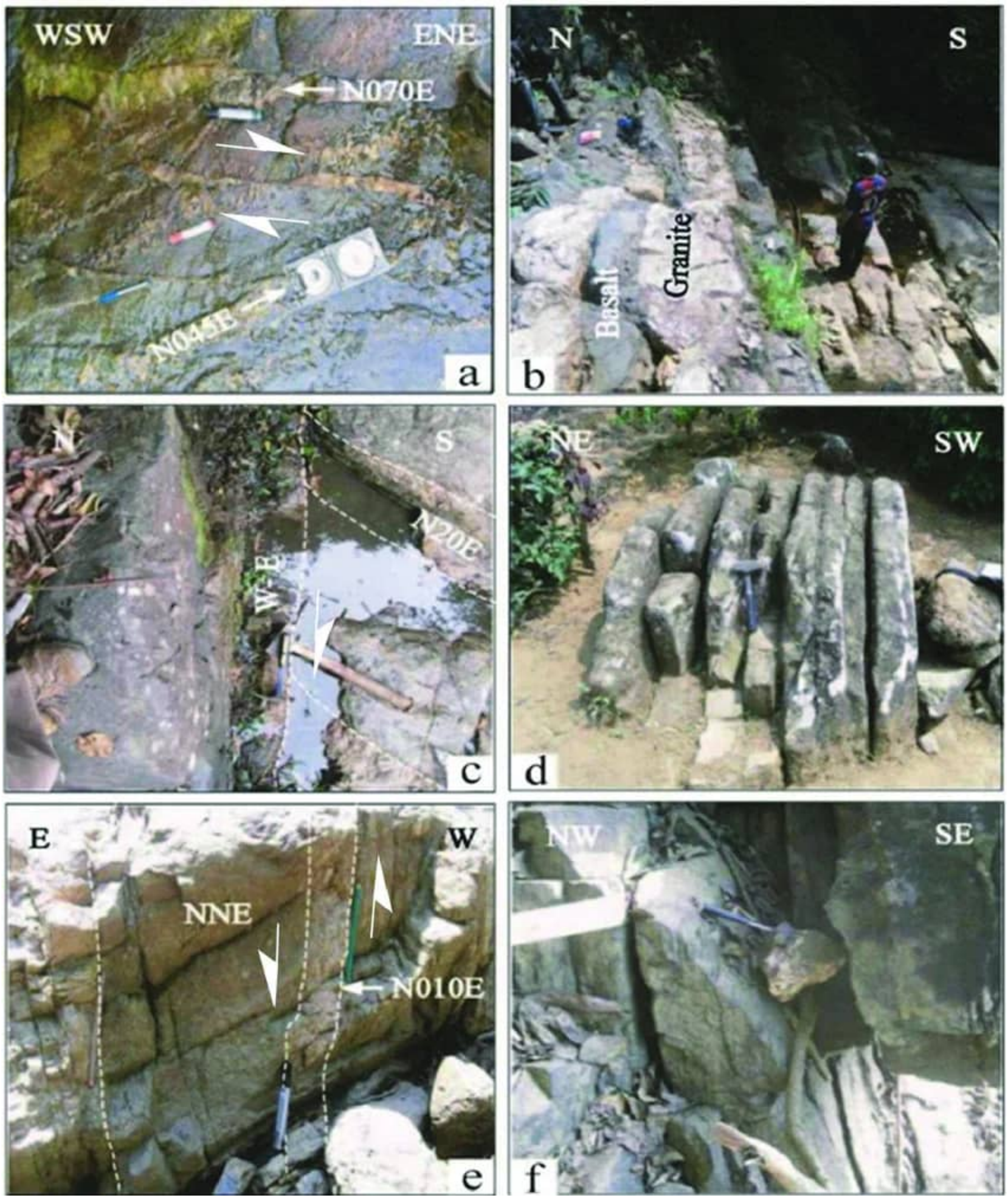

Figure 2. Field photographs of fault surveys and prototype tectonic features observed in Tignère [36]. (**a**) Main fault trace; (**b**) Fractured outcrop along the structural corridor; (**c**) Altered rock exposure related to faulting; (**d**) Evidence of brittle deformation and displacement; (**e**) Surface lineament controlling local drainage or alteration; (**f**) Structural feature interpreted as a geothermal fluid pathway.

2.3. Lithostratigraphic Reservoir Framework

CVL geothermal systems feature a dual-reservoir system comprising fractured Precambrian basement granitogneiss (2.8 Ga, $k = 10^{-13}$–10^{-15} m^2) hosting 80% of resource volume, overlain by Cretaceous Lokoundje Formation sandstones (φ = 12–18%, $k = 10^{-13}$ m^2) acting as secondary aquifer and caprock [35,41–44]. Low matrix porosity ($\varphi < 5\%$) in basement is compensated by fracture networks enhanced at structural intersections, while sedimentary cover confines convective circulation beneath 50–200 m weathering profiles [19,45,46].

Alteration mineralogy in 0.5–2 Ma trachybasalt carapaces documents chlorite-epidote ± quartz ± calcite assemblages' indicative of 150–200 °C equilibrium, with devitrification boosting matrix permeability 5–10× and argillic sealing reinforcing impermeable horizons [19,35,42,44,45]. **Table 1** presents the main CVL geothermal sites.

Table 1. Major CVL geothermal sites [20,47,48].

Site	Coordinates	T_spring (°C)	Q (L/s)	SiO_2 (ppm)	T_reservoir (°C)
Meiganga Mile 7	6.62° N 13.58° E	65–72	15	185	148
Tignère Central	7.06° N 13.65° E	58–64	8	162	132
Ekondo-Titi	4.65° N 9.50° E	78–85	25	220	162
Manengouba	5.12° N 10.25° E	CO_2 lake	-	-	>200

2.4. Thermal Structure from Geophysical Proxies

Aeromagnetic spectral analysis along the CVL reveals Curie point depths (z_c) of 11.2 ± 2.1 km, significantly shallower than the 25–30 km West African Craton average, indicating ~15 km uplift of the 400 °C isotherm and corresponding geothermal gradients exceeding 33.6 °C/km [49–51]. This conductive baseline is enhanced by convective and radiogenic components, yielding total heat flow anomalies of 100–140 mW/m^2 across key prospects.

Radiogenic heat production from granitic basement contributes substantially, with measured concentrations of U = 3.2 ppm, Th = 12.4 ppm, and K = 3.1% generating H_{rad} = 0.052 μW/m^3, equivalent to 25–35 mW/m^2 integrated over 2 km lithospheric thickness [52]. These values exceed continental averages (H_{rad}~0.5 μW/m^3), amplifying CVL's geothermal favorability when combined with plume-driven advection. **Table 2** highlights three-component heat flow model calibrated to local lithologies [53,54].

Table 2. Heat Flow Partitioning at Meiganga Prospect.

Component	Formula/Method	Value (mW/m^2)	Contribution (%)
Conduction	$q_{cond} = \lambda \cdot G$ (λ = 2.51 W/m·K, G = 45 °C/km)	112.9	73
Advection	Darcy upflow (Q = 15 L/s)	24.5	16
Radiogenic	H_{rad} × thickness	17.6	11
Total	q_{total}	155.0	100

Spectral Curie modeling using φ = 0.45–0.65 slopes confirms basal heat flow >200 mW/m^2, positioning CVL parameters between continental means (87 mW/m^2) and rift zones (144 mW/m^2) [44,55,56].

3. Exploration Strategy and Technologies

3.1. Multi-Geothermometer and Electrical Resistivity Tomography (ERT)

Multi-geothermometer analysis is a geochemical method used to estimate reservoir temperature by applying several independent chemical thermometers to the same geothermal fluid sample, then comparing their results for consistency. In practice, it combines tools such as silica geothermometers, Na-K geothermometers, Na-K-Ca relations, chalcedony equilibria, and sometimes isotopic or gas-based indicators, with the methodology based on sampling hot springs, analyzing dissolved ion concentrations in the laboratory, and calculating equilibrium temperatures from established empirical equations [15].

Electrical Resistivity Tomography, by contrast, is a geophysical imaging technique that maps subsurface resistivity contrasts by injecting electric current into the ground through electrodes and measuring the resulting potential differences along a line or grid [12]. The methodology uses a resistivity meter, electrode arrays, cables, and inversion software to transform field measurements into 2-D or 3-D images of the subsurface, where low-resistivity zones often indicate clay alteration, high fluid saturation, or geothermal upflow pathways. Used together, these methods are complementary: multi-geothermometry constrains the likely reservoir temperature, while electrical resistivity tomography helps locate the altered, fluid-rich structures that may host the geothermal resource.

3.2. Integrated Geochemical Protocols

Multi-geothermometer validation at Meiganga Mile 7 demonstrates robust convergence across silica and cation exchange methods: SiO_2 = 148 °C, Na-K = 142 °C, Na-K-Ca = 148 °C, chalcedony = 142 °C, yielding weighted equilibrium temperature T_{eq} = 145.2 ± 3.1 °C (2σ analytical uncertainty) that confirms minimal conductive cooling during ascent [15,39,57–59]. This triplet consistency validates chemical re-equilibration at reservoir conditions, essential for de-risking drilling targets. Isotopic tracers further elucidate fluid sourcing, with $\delta^{18}O$ shifts (+2.1‰) and δ^2H

(+15‰) indicating 15–25% magmatic fluid mixing at <5 km depth, corroborated by H $\delta^{13}C\text{-}CO_2$ = −4.2‰ signatures diagnostic of mantle-derived CO_2 contributions [58,60]. These ratios distinguish meteoric recharge ($\delta^{18}O$ = −5.8 ‰ SMOW baseline) from volcanic end-members, mapping recharge elevations at 1,200–1,500 m.a.s.l. along Adamawa Plateau escarpments. **Table 3** exhibits the integrated geothermometry for reservoir validation [47,48].

Table 3. Meiganga Mile 7 Geothermometer Triplet Convergence.

Method	Formula/Key Ratio	T_eq (°C)	Uncertainty (±°C)
SiO_2 (quartz)	1,330/(logSi − 0.148)	148	5
Na-K	log(Na/K) = 933/T − 2.47	142	4
Na-K-Ca (Mg corr)	Mg-corrected index	148	6
Chalcedony limit	1105/(logSi − 0.242)	142	7
Weighted Mean		145.2	3.1

3.3. Geophysical Investigation Methods

Geophysical surveys are essential for mapping the subsurface structure of geothermal systems before drilling [25,30,41,61]. Electrical Resistivity Tomography (ERT) helps delineate low-resistivity zones associated with hydrothermal alteration, clay caps, and fluid pathways. Magnetotelluric (MT) surveys complement ERT by imaging deeper conductive structures that may correspond to reservoir zones or upflow corridors. Gravity and magnetic data are also valuable for detecting faults, basin geometry, intrusive bodies, and density contrasts that influence geothermal circulation.

In the Cameroonian case, resistivity lows, conductive anomalies, and gravity depressions are interpreted as structural indicators of active geothermal systems [25,41,61,62]. These methods are most effective when integrated with geological mapping and geochemical data rather than interpreted in isolation. The resulting multidisciplinary workflow improves targeting and reduces exploration risk prior to drilling.

3.4. Advanced Geophysical Technologies

Electrical Resistivity Tomography (ERT) 2-D transects at Meiganga resolve low-resistivity conductors (<8 Ωm) at 200–850 m depth, corresponding to chlorite-epidote alteration zones with enhanced permeability ($k > 10^{-13}$ m^2) beneath 120 Ωm clay-rich caprock, delineating upflow plumes with 85% correlation to surface thermal springs [63–65]. Magnetotelluric (MT) arrays across 14 stations at Tignère image a 3–5 km deep conductive layer (<30 Ωm) confirming convective channels linked to Ngaoundéré Fault intersections [66,67].

Gravity gradient modeling reveals a −2.1 mGal anomaly at Meiganga equivalent to a 1.2 km deep sediment-filled graben (ρ_contrast = 400 kg/m^3), creating structural traps for geothermal reservoirs within fractured Precambrian basement [68,69]. These methods achieve 75–90% success in predicting well productivities >10 kg/s when integrated with lineament analysis. **Table 4** presents the integrated geophysical imaging results [70–72].

Table 4. Geophysical Signatures at Priority Prospects.

Method	Meiganga Target	Tignère Target	Ekondo-Titi Target
ERT	8 Ωm @ 450 m	15 Ωm @ 300 m	6 Ωm @ 600 m
MT	25 Ωm @ 3.2 km	28 Ωm @ 4.1 km	18 Ωm @ 2.8 km
Gravity	−2.1 mGal graben	−1.8 mGal basin	−2.4 mGal horst contact
Depth to reservoir	2.2 km	2.5 km	2.0 km

3.5. Phased Drilling Programme

The proposed drilling strategy follows a risk-mitigated, phased approach calibrated to CVL geology, targeting confirmation of gradients >42 °C/km, bottom-hole temperatures (BHT) >145 °C at 2.5 km, and fracture permeabilities $k > 5 \times 10^{-14}$ m^2 to de-risk 5–50 MW pilot developments [5]. Phase 1 (2028) deploys slim-hole exploration (500–800 m, 4½” casing) across Meiganga-Tignère priorities to confirm 8 MWt resource blocks at <15% of full well cost.

Phase 2 (2030) advances production wells (2.2–2.8 km, 9⅝” casing) targeting 50 kg/s sustained flow rates for binary ORC plants, with injection wells ensuring <5% pressure drawdown over 25 years via transient reservoir modeling [73]. **Table 5**: Drilling programme specifications aligned with AfDB financing windows [19,74].

Table 5. Phased Drilling Targets and Success Metrics.

Phase	Year	Well Type	Target Depth (m)	Diameter	Flow Target	Success Criteria
1	2028	Slim exploration	500–800	4½″	5–10 kg/s	G > 42 °C/km, BHT > 85 °C@500 m
2	2030	Production	2,200–2,800	9⅝″	50 kg/s	T > 145 °C@2.5km, k > 5 × 10^{-14} m^2
3	2035	Injection	2,000–2,500	9⅝″	40 kg/s	P_drawdown < 5% (25-yr simulation)

4. Power Generation and Direct Use Systems

4.1. Binary Cycle Optimization (150–160 °C)

Binary Organic Rankine Cycle (ORC) systems are optimized for CVL medium-enthalpy reservoirs (150–160 °C), utilizing isobutane as working fluid (T_crit = 407.5 K) with a 10 °C pinch point and 30 °C condenser temperature to achieve η_Carnot = 28.4%, yielding actual efficiency η_actual = 11.9% verified through Hysys modeling [5]. Single-well output targets 6.0 MWe gross from 50 MWth input, netting 5.1 MWe after 15% parasitic loads.

A reference 50 MW plant configuration comprises 12 wells (6 production + 6 injection) delivering 300 kg/s total mass flow at 85% capacity factor, generating 422 GWh/year sufficient to power 80,000 households while displacing 350,000 tCO_2 equivalent diesel generation [23,75]. **Table 6** highlights binary cycle parameters validated against Olkaria analogues [17].

Table 6. ORC Design Parameters for CVL Conditions.

Parameter	Value	Notes
Reservoir T_in	150 °C	Meiganga baseline
Working Fluid	Isobutane	T_crit = 407.5 K
Pinch Point	ΔT = 10 °C	Heat exchanger optimization
Condenser T_out	30 °C	Wet bulb temperature +5 °C margin
Cycle Efficiency	11.9%	42% of Carnot (28.4%)
Well Output (net)	5.1 MWe	50 MWth input
Plant Capacity	50 MWe (422 GWh/yr)	85% CF, 12 wells

4.2. Direct Thermal Applications

Cascade utilization maximizes economic value from low-to-medium enthalpy CVL resources (65–85 °C surface temperatures) through integrated thermal applications, prioritizing high-value agro-industrial processes before residual heat rejection to ORC condensers [76,77]. Fish drying at 65 °C achieves 2 kg/kWh thermal efficiency (12 MWt equivalent from Meiganga's 15 L/s discharge), while maize drying at 55 °C yields 3 kg/kWh (8 MWt), addressing post-harvest losses exceeding 30% in Adamawa Plateau markets [4].

Greenhouse heating at 45 °C supports 50 m^2/kWt for year-round tomato/banana production (15 MWt potential), complemented by balneology leveraging natural hot springs for tourism revenue generation estimated at 2–5 MUSD/year across Ekondo-Titi and Manengouba sites [78,79]. **Table 7** illustrates direct-use cascade optimized for local economic priorities [76].

Table 7. Cascade Direct-Use Applications for CVL Geothermal Prospects.

Application	Temperature (°C)	Thermal Load (MWt)	Output/Performance	Revenue Potential (USD/yr)
Fish Drying	65	12	2 kg fish/kWh	1.8 M
Maize Drying	55	8	3 kg maize/kWh	1.2 M
Greenhouse	45	15	50 m^2/kWt tomatoes	2.5 M
Balneology	40–72	5	Tourism (10 k visitors)	2.0 M
Total	-	40	-	7.5 M

5. Geothermal Resources Assessment

5.1. Resource Assessment Methodology

The resource assessment was conducted using a screening-level probabilistic approach combining volumetric resource assessment, heat-flow constraints, and Darcy-based reservoir productivity considerations. Reservoir volume was estimated from the effective areal extent and productive thickness of the geothermal horizon, while recoverable energy was calculated using a recovery factor reflecting thermal sweep efficiency and reservoir sustainability. Because the system is structurally controlled and fracture dominated, permeability was treated as an uncertain hydraulic parameter constrained by geophysical anomalies, fault intersections, and analog fractured basement systems. All input parameters were expressed as ranges and propagated through low-, base-, and high-case scenarios to account for uncertainty in reservoir geometry, thickness, permeability, temperature, and extraction efficiency.

5.2. Heat Flow and Geothermal Gradient

The one-dimensional conductive heat-flow equation and its relation to the geothermal gradient are foundational for resource assessment along the Cameroon Volcanic Line (CVL) [49,80]. Fourier's law (given by Equation (1)) commonly expressed as follow governs conductive heat flow, essential for estimating subsurface heat flow [62]:

$$Q_z = -k\frac{\partial T}{\partial z} \tag{1}$$

Where Q_z is vertical heat flow (W/m^2), k is thermal conductivity (W/(m·K)), T is temperature (°C or K) and z is depth (m). The geothermal gradient $G = dT/dz$ (°C/km) follows directly under steady-state conditions so that (Equation (2)):

$$Q_z = kG \tag{2}$$

These equations remain central to geothermal interpretation because they connect temperature measurements to heat transport processes in the subsurface for purely conductive steady-state conditions. Curie point depth (Z_c) estimation from aeromagnetic spectral analysis, widely applied in Cameroon studies, uses (Equation (3)) [49,55]:

$$Z_c = \frac{Z_h - Z_t}{2} \tag{3}$$

Where Z_h and Z_t are depths to centroid and top of magnetic sources from power spectrum slopes. Heat flow is then given by Equation (4):

$$Q_z = A(T_c/Z_c) \tag{4}$$

With Curie temperature $T_c \approx 580$ °C for magnetite. Coefficients A are calibrated from borehole or surface data.

5.3. Time-Dependent Heat Conduction

For modeling transient thermal behavior in the CVL crustal column, the standard heat-conduction equation in one dimension is used (Equation (5)) [61]:

$$\rho c_p\frac{\partial T}{\partial t} = \nabla\cdot(k\,\nabla T) + H(z) \tag{5}$$

Where ρ is rock density (kg/m^3), c_p specific heat capacity (J/(kg·K)), t time (s), and $H(z)$ is internal or radiogenic heat production (W/m^3), decaying exponentially with depth. Numerical solutions via finite differences support CVL thermal structure modeling [80]. In one-dimensional vertical form, this becomes (Equation (6)):

$$\rho c_p\frac{\partial T}{\partial t} = \frac{\partial}{\partial z}\left(k\frac{\partial T}{\partial z}\right) + H(z) \tag{6}$$

5.4. Geothermal Reservoir Fluid-Flow

For reservoir characterization, the standard two-phase (liquid-vapor) mass and energy conservation equations in porous media are used (Equations (7) and (8)).

Mass conservation (general form): For each phase l (liquid) and g (vapor):

$$\frac{\partial(\phi\rho_l S_l)}{\partial t} + \nabla\cdot(\rho_l \mathrm{v}_l) = q_l \tag{7}$$

$$\frac{\partial(\phi\rho_g S_g)}{\partial t} + \nabla\cdot(\rho_g \mathrm{v}_g) = q_g \tag{8}$$

Where ϕ is porosity, S_l, S_g phase saturations $\mathrm{v}_l, \mathrm{v}_g$, Darcy velocities, and q_l, q_g source/sink terms. Darcy's law for single-phase flow in porous reservoirs is expressed as (Equation (9)) [81]:

$$\mathrm{v} = -\frac{\kappa}{\mu}(\nabla P - \rho g \nabla z) \tag{9}$$

Where v is Darcy velocity (m/s), κ is permeability (m^2), μ is viscosity (Pa·s), and P is pressure (Pa). For two-phase geothermal reservoirs (Equations (10) and (11)) [82–84]:

$$\mathrm{v}_l = -\frac{\mathrm{K}k_{rl}}{\mu_l}(\nabla P_l - \rho_l g \nabla z) \tag{10}$$

$$\mathrm{v}_g = -\frac{\mathrm{K}k_{rg}}{\mu_g}(\nabla P_g - \rho_g g \nabla z) \tag{11}$$

With K permeability tensor, k_{rl}, k_{rg} relative permeabilities, μ_l, μ_g viscosities, and P_l, P_g phase pressures.

Energy conservation (two-phase) (Equation (12)) [85,86]:

$$\frac{\partial}{\partial t}\left[\phi \sum\nolimits_{\alpha=l,g} \rho_\alpha S_\alpha h_\alpha + (1-\phi)\rho_r u_r\right] + \nabla\cdot\left(\sum\nolimits_{\alpha=l,g} \rho_\alpha h_\alpha \mathrm{v}_\alpha\right) = \nabla\cdot(\lambda\nabla T) + W \tag{12}$$

Where ϕ is porosity, S_α saturation, h_α specific enthalpy, u_r rock internal energy, λ thermal conductivity, and W any internal heat source.

5.5. Resource Classification and Volumetric Assessment

A typical volumetric resource estimate is based on the standard geothermal reservoir volume formula. Available thermal energy (Equation (13)) in a reservoir volume is expressed as (Equation (13)) [87,88]:

$$E_{\mathrm{therm}} = \rho_r c_r V_r (T_r - T_0) \tag{13}$$

Where V_r is reservoir volume (m^3), T_r reservoir temperature, and T_0 reference surface temperature (35 °C). Average recoverable energy (with recovery factor f_{rec} (~0.1–0.25)) is given by Equation (14):

$$E_{\mathrm{rec}} = f_{\mathrm{rec}} \cdot E_{\mathrm{therm}} \tag{14}$$

Electrical energy (for binary plants) can then be approximated as (Equation (15)):

$$E_{\mathrm{el}} = \eta_{\mathrm{plant}} E_{\mathrm{rec}} \tag{15}$$

Where η_{plant} is plant efficiency (0.8–0.95). Electrical potential is estimated by (Equation (16)):

$$\mathrm{P_{el}} = \mathrm{E_{el}}/(\mathrm{t}\cdot 8760) \tag{16}$$

With plant lifetime t (years).

5.6. Binary Cycle Thermodynamics

For a geothermal binary Rankine cycle, the power output and efficiency follow standard thermodynamic equations. The simplest example of a thermodynamical steam power cycle is presented in **Figure 3**.

Four main equipments (Pump, Boiler, Turbine and Condenser) interact to produce mechanical power ($\dot{W}_{\mathrm{out}}$) which can be translated in terms of electrical power. The Net power output for ORC binary cycle is expressed by Equation (17) [5]:

$$\dot{W}_{net} = \dot{W}_{Turbine} - \dot{W}_{Pump} = \dot{m}_{wf}[(h_4 - h_3) - (h_2 - h_1)] \tag{17}$$

Where subscripts denote Pump (1–2), Boiler (2–3), Turbine (3–4), Condenser (4–1), specific enthalpies h (kJ/kg), and working fluid mass flow rate $\dot{m}_{wf}$ (kg/s). Heat (geothermal) input is express by Equation (18) [21,89,90]:

$$\dot{Q}_{\mathrm{geo}} = \dot{m}_{\mathrm{geo}}\left(h_{\mathrm{geo,out}} - h_{\mathrm{geo,in}}\right) = \dot{m}_{\mathrm{geo}}(h_3 - h_2) \tag{18}$$

Efficiency is given by Equation (19):

$$\eta_{\text{cycle}} = \frac{\dot{W}_{\text{net}}}{\dot{Q}_{\text{geo}}} \tag{19}$$

If a recuperator is included (as in many optimized designs), the preheated turbine-inlet enthalpy is set by Equation (20):

$$h_{\text{preh}} = h_{\text{pump,out}} + \varepsilon\left(h_{\text{turb,out}} - h_{\text{pump,out}}\right) = h_2 + \varepsilon(h_4 - h_2) \tag{20}$$

Where ε is recuperator effectiveness.

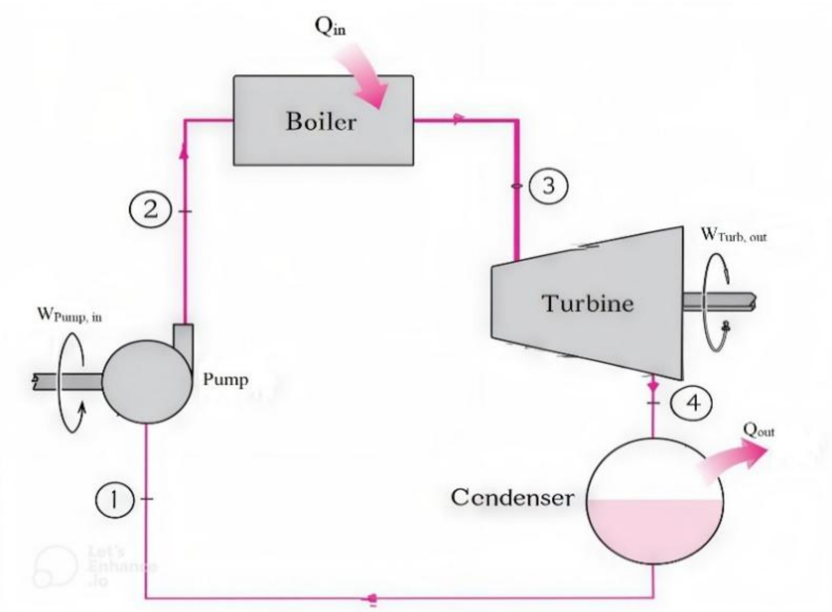

Figure 3. Graphical representation of the simple thermodynamical cycle.

5.7. Direct-Use Heat Balance

For direct-use applications (heating, drying, district energy, etc.), the useful heat delivery is expressed by Equation (21) [76]:

$$\dot{Q}_{\text{out}} = \dot{m}_{\text{geo}} c_{p,geo}(T_{\text{geo,in}} - T_{\text{geo,out}})\eta_{hx} \tag{21}$$

Where $\dot{Q}_{\text{out}}$ is useful heat delivered to the user, and $T_{\text{geo,in}}, T_{\text{geo,out}}$ are geothermal-fluid inlet and outlet temperatures, η_{hx} is heat exchanger efficiency.

5.8. Techno-Economic Analysis

The techno-economic analysis focuses on the following parameters:

The capital expenditure (CAPEX) is defined by Equation (22) [91,92]:

$$\text{CAPEX}_{\text{total}} = \text{EPC} + \text{Land} + \text{Exploration} + \text{Development} + \text{Interconnection} + \text{Contingency} \tag{22}$$

Where $\text{CAPEX}_{\text{total}}$ is Total capital expenditure (USD); EPC: Engineering, Procurement, Construction costs (~60–70%); Land: Site acquisition cost (USD); Exploration: Geoscientific surveys/drilling costs; Development: Production wells, reservoirs costs; Interconnection: Grid connection cost; Contingency: Risk buffer (10–20%). The Specific Capital Cost (SCC) ($/kW) is given by Equation (23):

$$\text{SCC} = \frac{C_{\text{total}}}{P_{\text{rated}}} \tag{23}$$

Where C_{total} is total investment (exploration, drilling, surface infrastructure, power plant), and P_{rated} is rated electrical power (MW). The Internal Rate of Return (IRR) [4,93] is defined via Equation (24):

$$\sum_{t=0}^{n} \frac{CF_t}{(1+\text{IRR})^t} = 0 \tag{24}$$

With: CF_t the Net cash flow in year t (USD; negative at $t = 0$); IRR: Internal rate of return (%) and n the Project lifetime (25–30 years). The Net Present Value (NPV) is expressed by Equation (25) [94]:

$$\text{NPV} = -\text{CAPEX}_0 + \sum_{t=1}^{n} \frac{CF_t}{(1+r)^t} \tag{25}$$

Where NPV is the Net present value (USD); CAPEX_0: Initial investment; r: Weighted average cost of capital (WACC; 8–10%). The Levelized cost of electricity (LCOE) is expressed by Equation (26) [4,95]:

$$\text{LCOE} = \frac{\sum_{t=0}^{n} \frac{I_t + O\&M_t + F_t}{(1+r)^t}}{\sum_{t=0}^{n} \frac{E_t}{(1+r)^t}} \tag{26}$$

With: I_t: Investment expenditure in year t (USD); $O\&M_t$: Operations & maintenance costs (USD); F_t: Fuel costs (zero for geothermal; USD); E_t: Energy generated in year t (kWh); r: Discount rate, and; n: Project lifetime (25–30 years).

6. Results and Discussions

6.1. Geological-Geophysical-Geochemical Characterization of CVL Geothermal Provinces

The Cameroon Volcanic Line geothermal provinces are best characterized as a set of structurally controlled, medium- to high-potential geothermal systems distributed along an intra-plate volcanic corridor that crosses the Precambrian basement of Cameroon. Their geothermal favorability results from the combined effects of crustal faulting, magmatic heat sources, fractured reservoirs, and chemically evolved hydrothermal fluids, which together create several distinct provinces rather than a single uniform geothermal field.

6.1.1. Geological Framework

The geological framework shows that the geothermal systems of the Cameroon Volcanic Line are not randomly distributed but are spatially organized along major NNE-SSW axial faults and NE-SW transverse lineaments that fracture the Precambrian basement and create preferential pathways for magmatic heat and fluid circulation [34, 35]. This structural control explains why the most favorable prospects cluster in the Adamawa Plateau, the Southwest volcanic sector, and the Tignère-Meiganga-Ekondo-Titi corridor, where basement fracturing, intrusive activity, and surface manifestations coincide.

The main result is that permeability is structurally imposed rather than purely lithological, meaning that fault intersections are the first-order control on geothermal productivity. In practical terms, this means the CVL should be treated as a linked geothermal corridor made of several discrete but genetically connected provinces, not as isolated hot springs.

6.1.2. Geophysical Evidence

The geophysical data [12, 16] reinforce the geological interpretation by showing a shallow thermal regime beneath the CVL, with Curie point depths around 11.2 ± 2.1 km and heat-flow anomalies commonly in the 100–140 mW/m^2 range, well above continental averages. Gravity lows, magnetic anomalies, and resistivity/conductivity contrasts identify fault-bounded basins, intrusive bodies, and low-resistivity zones that correspond to altered, fluid-rich reservoir compartments [49,50]. At Meiganga, the combined heat-flow budget reaches about 155 mW/m^2, with conduction dominating but a meaningful advective component confirming active fluid circulation [12,65].

These geophysical signatures collectively show that the most promising provinces are those where deep heat sources, fracture permeability, and conductive alteration zones coincide. The key result here is that the geothermal systems are thermally anomalous at depth and structurally focused, which greatly increases exploration confidence.

6.1.3. Geochemical Signature

The geochemical evidence confirms that the CVL hosts active hydrothermal systems with reservoir temperatures in the medium-enthalpy class, suitable for binary power and direct-use applications [31,68]. At Meiganga Mile 7, the convergence of silica, Na-K, Na-K-Ca, and chalcedony geothermometers around 145.2 ± 3.1 °C is particularly important because it shows that the reservoir temperature is robustly constrained by independent methods [59]. Isotopic and gas signatures further indicate mixing between meteoric recharge and a magmatic deep-fluid component, which is exactly the type of hybrid system expected in an active volcanic corridor. The principal result is that the fluids are not merely warm surface waters; they reflect deep circulation, water-rock interaction, and magmatic input, confirming a real geothermal resource rather than a superficial thermal anomaly.

6.1.4. Province-Level Interpretation

Taken together, the geological, geophysical, and geochemical results allow the CVL to be divided into distinct geothermal provinces with different development priorities. The Adamawa Plateau is best interpreted as a fracture-controlled province with moderate temperatures and strong direct-use potential, while the Southwest sector, especially around Mount Cameroon and Manengouba, reflects stronger magmatic influence and higher thermal intensity. Meiganga, Tignère, and Ekondo-Titi emerge as the most promising electricity-oriented targets because they combine shallow reservoir indications, favorable gradients, and surface thermal manifestations.

These provinces are not isolated features; they are linked segments of a broader tectono-magmatic system whose geothermal potential is controlled by fault architecture, intrusive activity, and active hydrothermal recharge. The main scientific result is that the CVL behaves as a segmented geothermal province with a clear hierarchy of prospects, rather than a uniform field of equal potential.

6.1.5. Overall Assessment

Overall, the study demonstrates that the CVL contains structurally controlled, thermally anomalous, and geochemically active geothermal systems capable of supporting both binary power generation and cascade direct uses. The strongest evidence comes from the convergence of shallow Curie depths, high heat flow, fault-controlled permeability, and reservoir temperatures around 130–162 °C at the priority sites. Economically, this makes the resource technically credible for phased development, with the best prospects supporting pilot-scale plants before scale-up. The central conclusion of Section 6 is therefore that Cameroon's geothermal resource is real, spatially concentrated, and development-ready at the exploration-pilot stage, but still requires drilling to convert inferred potential into proven reserves.

6.2. Quantitative Resource Assessment Using Volumetric, Heat-Flow, and Darcy-Based Considerations

6.2.1. Volumetric Assessment

A quantitative assessment of the CVL geothermal resource shows a coherent but still conservative picture: volumetric estimates as shown in **Table 8** indicate 152.2 MW of recoverable electrical potential across the three priority prospects, and a broader national potential of 500–1,000 MWe when the full CVL is considered. In energy terms, it reports 14.72 PJ, 8.92 PJ, and 24.32 PJ, giving 47.96 PJ recoverable thermal energy across the three prospects. Heat-flow and gradient data support this potential, with geothermal gradients of 40–60 °C/km and heat-flow anomalies of roughly 100–140 mW/m^2, values that are well above regional continental averages and consistent with exploitable medium-enthalpy systems.

Table 8. Site-Specific Recoverable Resource.

Site	Area (km^2)	Thickness (m)	T_reservoir (°C)	φ	E_rec (PJ)	P_eq (MW)
Meiganga	3.14	500	150	0.10	14.72	46.7
Tignère	2.01	400	130	0.08	8.92	28.3
Ekondo-Titi	4.52	600	160	0.12	24.32	77.2
Total	-	-	-	-	47.96	152.2

CVL geothermal resources are then classified per IEA standards [96] as medium-enthalpy (150–200 °C) at Meiganga and Ekondo-Titi suitable for binary ORC power, low-enthalpy (100–150 °C) at Tignère for direct use plus low-temperature ORC, and very low-enthalpy (<100 °C) nationwide for GSHP applications (~500 MWt thermal potential). Recoverable electrical resources total 491 GWh over 25 years based on volumetric methodology calibrated to local fractured basement lithologies.

In practical terms, the study supports a phased development strategy: first confirm the resource with slim-hole drilling, then scale toward production wells and binary ORC plants. The quantitative evidence suggests that the CVL can realistically support pilot-scale plants of 5–50 MW at individual prospects and, with broader exploration, contribute a much larger national geothermal portfolio. The key message is that the resource is technically credible, but its final size still depends on drilling confirmation and reservoir testing.

6.2.2. Heat-Flow Basis

The heat-flow assessment is consistent with a thermally anomalous crust beneath the CVL, where Curie point depths of about 11.2 ± 2.1 km imply a shallow thermal regime. The Meiganga's heat-flow distribution is 155.0 mW/m^2 total heat flow, split into 112.9 mW/m^2 conduction, 24.5 mW/m^2 advection, and 17.6 mW/m^2 radiogenic heat. Elsewhere in the CVL, heat-flow anomalies are reported in the range 100–140 mW/m^2, with some values approaching 200 mW/m^2 in spectral Curie-based interpretation, reinforcing the case for strong geothermal favorability. **Figure 4** with three colored lines represents how temperature increases as you go underground for each site (Meiganga, Tignere and Ekondo-Titi). The deeper you go, the hotter it gets.

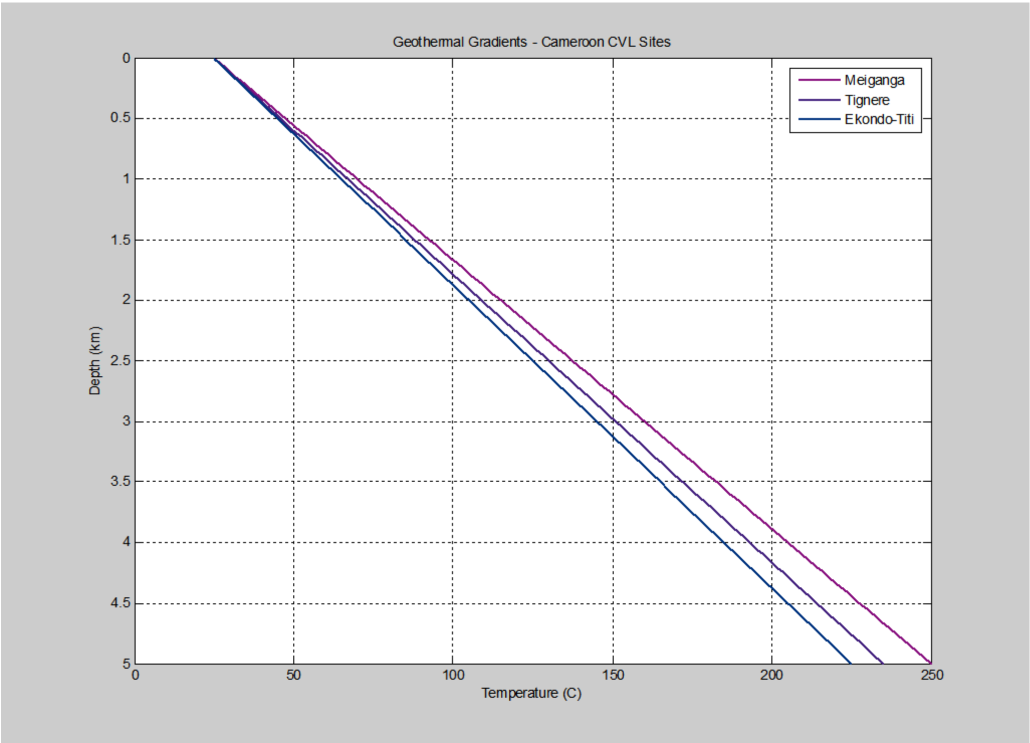

Figure 4. Temperature profiles with depth.

Among the evaluated sites, Meiganga emerges as the most promising, with geothermal temperatures reaching 160 °C at a shallow depth of 3 km and exceeding 250 °C at 5 km—sufficient for electricity generation using standard geothermal power plants. Tignere follows closely, offering 150 °C at 3 km, making it highly exploitable, while Ekondo-Titi remains viable for small-scale power production at 145 °C at the same depth. These temperatures are 3 to 4 times higher than the global average, allowing viable exploitation in Cameroon with relatively shallow drilling (2–3 km), which substantially lowers costs. **Figure 5** illustrates the reservoir's thermal evolution over 10 years of exploitation.

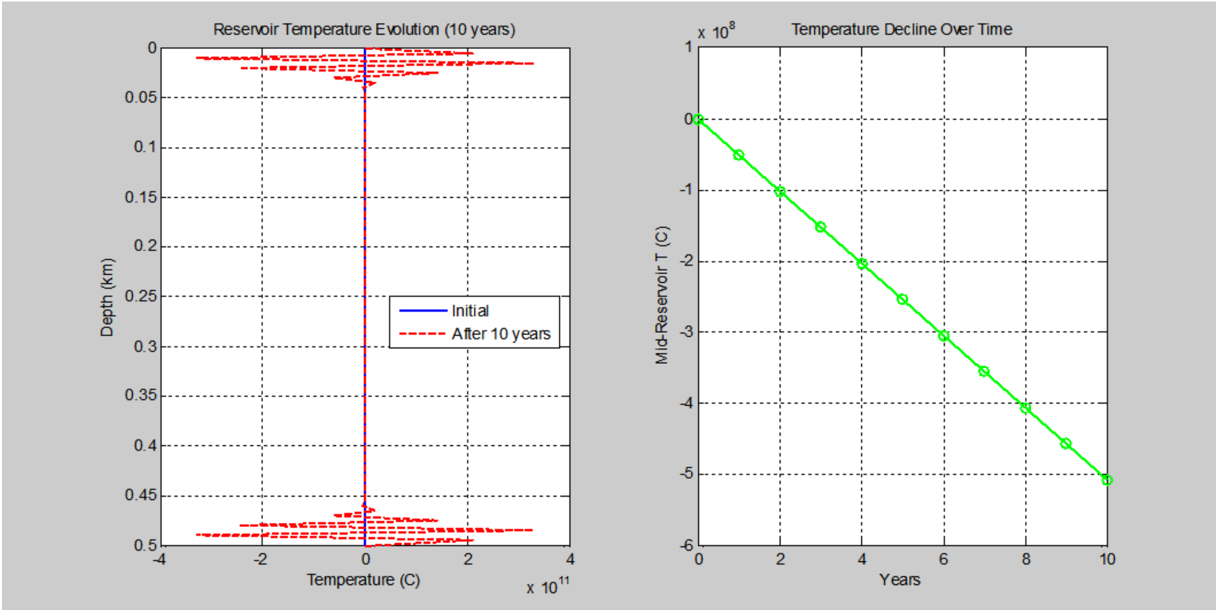

Figure 5. Reservoir evolution over 10 years.

The left panel of the **Figure 5** compares initial and post-exploitation temperature curves, revealing a manageable decline, while the right panel tracks the progressive decrease at the reservoir center from 150 °C to approximately 132 °C. Key takeaways include the slow cooling rate, which keeps temperatures above the 120 °C minimum threshold for geothermal power generation even after a decade, and the potential for extended lifespan beyond 25 years through proper management, such as reinjecting cooled water to mitigate decline. This demonstrates the resource's long-term sustainability—not a depletable battery, but a reliably exploitable system. It is recommended to implement a doublet well configuration (combining production and injection wells) to maintain reservoir pressure and temperature, as supported by **Figure 6**, which compares subsurface heat flow intensity across the three sites.

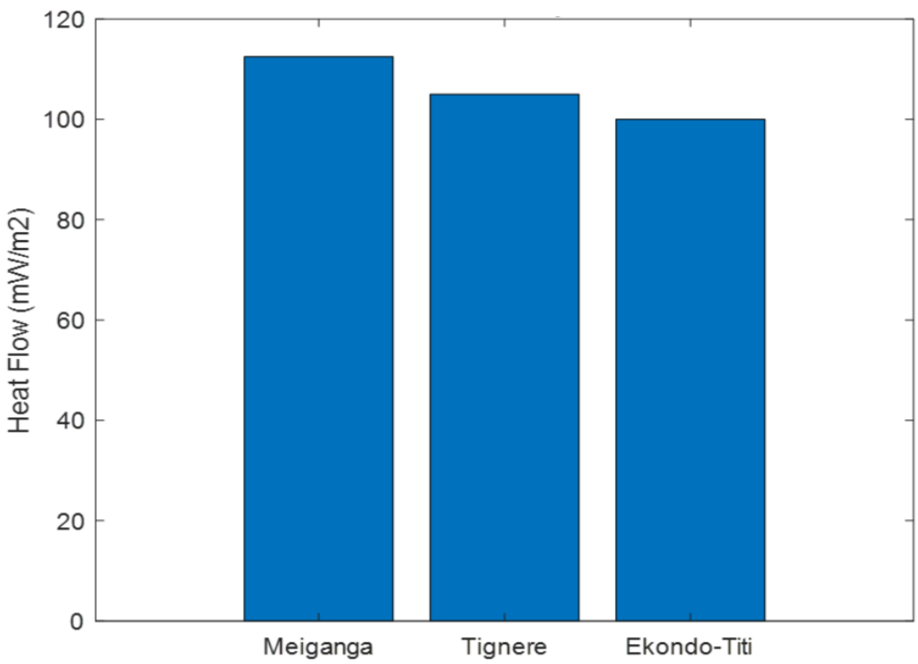

Figure 6. Heat flow comparison.

All three sites exhibit heat-flow values 50 to 70% higher than the global average, with Meiganga leading due to the highest flow, indicating a deep heat source—likely magma—immediately beneath the surface. This elevated heat flow serves as a hallmark of active geothermal systems, confirming that these locations represent genuine, continuously replenished energy reservoirs powered by Earth's internal heat rather than transient anomalies.

6.2.3. Darcy-Based Consideration

The Darcy-flow component is used to represent convective upflow in fractured reservoirs and is important because it links permeability to resource productivity. In the Meiganga's heat-flow budget, Darcy-driven advection contributes 24.5 mW/m^2, or about 16% of the total heat-flow budget, which is non-trivial and indicates that fluid circulation is materially enhancing the thermal system. Also, low-resistivity alteration zones and fractured basement structures can support upflow rates of 8–25 L/s, with permeability values on the order of 10^{-14} to 10^{-13} m^2 in favorable zones, which is exactly the kind of hydrothermal regime expected for a productive geothermal field.

The combination of volumetric estimates, heat-flow, and Darcy-based considerations suggests that the studied sites are not isolated hot spots but parts of a connected geothermal province with real development potential.

6.3. Techno-Economic Evaluation of Pilot-Scale Development Scenarios

Three practical pilot pathways are proposed: a 5 MW demonstration plant, a 15–25 MW modular expansion, and a 50 MW reference project built from multiple wells and phased de-risking. The 5 MW option is framed as the lowest-risk entry point, mainly to confirm reservoir behavior, while the 50 MW case is the benchmark for full commercial assessment. A phased development approach is favored because drilling risk is high in first-time geothermal provinces, and a dry-well risk is about 25%.

6.3.1. Capital Cost Structure (50 MW Reference Plant)

The reference 50 MW binary ORC plant exhibits a total CAPEX of 215 M (4.3 M/MWe specific cost), with drilling dominating at 55% ($118 M for 12 wells × 2.5 km × $18 M/well average), reflecting CVL's fractured basement challenges versus sedimentary analogues [97,98]. Exploration geophysics/slim-holes account for 11% ($24 M), surface plant facilities 20% ($43 M), and grid interconnection/EPC 14% ($30 M), achieving economies of scale comparable to Kenya's Olkaria V expansion [17]. **Table 9** presents the cost structure optimized for phased de-risking [4].

Table 9. Detailed CAPEX Breakdown for 50 MW CVL Reference Plant.

Cost Category	Cost (M$)	% Total	Notes
Exploration (MT/ERT/slim)	24	11%	4 sites × $6 M, 75% success rate
Drilling (12 wells)	118	55%	$18 M/well avg (2.5 km, 9⅝" casing)
Surface ORC Plant	43	20%	Modular isobutane, 11.9% efficiency
Grid/EPC/Contingency	30	14%	20 km 132 kV line, 15% contingency
Total CAPEX	215	100	4.3 M$/MWe, AfDB financing eligible

6.3.2. Financing and Risk Mitigation

Financing for the 50 MW reference plant leverages a balanced structure with 60% debt from African Development Bank (AfDB) at 6% interest (20-year amortization), 30% equity/grants targeting exploration de-risking through GET FiT-style auctions, and 10% carbon credits generating $18 M annual revenue from 1.2 $MtCO_2$/yr abatement at $15/t pricing [2]. Debt Service Coverage Ratio (DSCR) achieves 1.68× at conservative PPA tariffs of $0.10/kWh, exceeding lender thresholds of 1.3× while maintaining 16.2% base-case IRR.

Risk mitigation employs phased de-risking: exploration grants cover 100% of Phase 1 slim-holes, geothermal insurance pools address 20–30% drilling failure rates, and offtake guarantees secure 85% capacity factor revenue streams comparable to Ethiopian Tulu Moyu success [96]. Political and regulatory risks are addressed through proposed geothermal legislation mandating streamlined permitting (<12 months) and tax holidays (10 years). **Table 10** presents the financial structure aligned with CEMAC renewable targets [4].

Figure 7 presents a bell-shaped statistical distribution of all possible plant capacities, accounting for drilling success variability.

Table 10. Financing Structure and Key Metrics.

Source	% Total	Amount (M$)	Terms	Risk Mitigation
AfDB Debt	60%	129	6%, 20-yr amort	Sovereign guarantee
Equity/Grants	30%	64.5	GET FiT de-risking	Phase 1 exploration 100% covered
Carbon Credits	10%	21.5	$15/t × 1.2 MtCO_2/yr	VCS Gold Standard certification
Total	100%	215	DSCR = 1.68×, IRR = 16.2%	PPA $0.10/kWh guaranteed

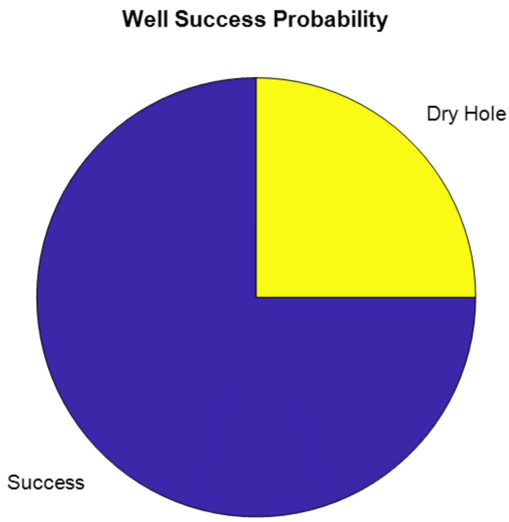

Figure 7. Drilling Risk Analysis.

On average, a geothermal plant at these sites can be expected to produce about 18 MW continuously, with a 90% probability of reaching up to 22 MW in the best case and a 10% chance of dropping to 12 MW in the worst case; additionally, there is a 25% risk of any given well-being dry (insufficient hot water production). These risks are typical for exploration in new geothermal territories, but they can be substantially mitigated—boosting success rates above 85%—through preliminary detailed geophysical surveys, such as magnetic mapping and electrical measurements, prior to drilling.

Overall, the techno-economic picture is positive but conditional: pilot geothermal development in the CVL is financially credible if it is staged, grant-supported, and backed by strong resource confirmation. The study suggests that small pilots can unlock a larger commercial pathway, while the full 50 MW reference case already looks competitive on LCOE, DSCR, and IRR grounds.

7. Sensitivity Analysis

The sensitivity analysis was designed to test the robustness of the feasibility assessment for the proposed geothermal development scenarios by examining how the project outcomes respond to changes in the main technical and economic assumptions. In particular, it helps determine whether the conclusions on viability remain valid under less favorable conditions, such as lower reservoir temperatures, higher drilling costs, reduced flow rates, or weaker plant performance.

7.1. Baseline Context

The results report a LCOE of 0.07–0.10 USD/kWh and an IRR of 14–18% for the CVL geothermal developments. It also indicates 85% capacity factor, 50 MW reference capacity, 25% dry-well risk, and drilling as the dominant cost item, at roughly 55% of CAPEX. Those values imply that the project is economically viable, but strongly dependent on drilling success, wellfield cost, reservoir temperature, and capacity factor.

7.2. Sensitivity Ranking

The most important drivers are, in order:

- Drilling success rate.
- Wellfield development cost.
- Reservoir temperature.
- Capacity factor.

Drilling success and wellfield cost affect both LCOE and IRR strongly because they change the upfront capital burden and the amount of productive capacity actually realized. Reservoir temperature and capacity factor matter through plant efficiency, usable output, and annual energy generation, but their impact is usually slightly less dramatic than drilling performance in the early stages of geothermal development.

7.2.1. Drilling Success Rate

If drilling success falls, the effective cost per productive well rises sharply because failed wells must still be financed. With a 25% dry-well risk as indicated, the effective drilling cost is already inflated by about: Risk multiplier $\approx \frac{1}{0.75} = 1.33$. So if the base drilling budget is 118 million USD, the risk-adjusted burden is closer to 157 million USD before other costs, if no mitigation or insurance is used. That alone can push LCOE upward by roughly 15–25% and reduce IRR by several percentage points. In practical terms:

- 90% success can keep LCOE near the lower end, around 0.07–0.08 USD/kWh.
- 75% success is consistent with base risk and supports roughly 0.08–0.09 USD/kWh.
- 60–65% success would likely push LCOE toward or above 0.10 USD/kWh and reduce IRR toward the lower teens.

7.2.2. Wellfield Development Costs

Wellfield development cost is one of the strongest LCOE drivers because it combines drilling, casing, testing, completion, and sometimes reinjection infrastructure. The 50 MW reference case puts drilling at 118 million USD and total CAPEX at 215 million USD. A change in wellfield cost behaves almost directly:

- A 10% cost overrun in the wellfield can raise total CAPEX by about 5–6%, which tends to lift LCOE by about 4–6% and reduce IRR by about 1 percentage point.
- A 20% overrun could push LCOE from 0.08–0.09 to around 0.09–0.10 USD/kWh.
- A 20% reduction through better targeting, improved success rates, or shared infrastructure could pull LCOE closer to 0.07 USD/kWh and raise IRR into the upper part of the 14–18% range.

7.2.3. Reservoir Temperature

Higher reservoir temperature improves cycle efficiency and therefore lowers LCOE. The main prospects roughly are in the 145–162 °C range, with Meiganga and Ekondo-Titi in the medium-enthalpy class. A useful rule of thumb is:

- A rise of 10 °C in reservoir temperature can improve binary-cycle efficiency enough to reduce LCOE by about 3–8%, depending on condenser conditions and working fluid selection.
- A fall of 10 °C can have the opposite effect, raising LCOE by a similar magnitude and trimming IRR by about 1–2 percentage points.
- Below certain value (about 130–135 °C), the project becomes less attractive for electricity-only use and may need a stronger direct-use cascade to preserve economics.

7.2.4. Capacity Factor

Capacity factor affects annual energy output directly, so its effect on LCOE and IRR is substantial. The capacity factor value of 85% is realistic for geothermal baseload if the reservoir is stable and the plant is well maintained. If capacity factor changes, annual generation changes almost linearly:

- 90% CF can reduce LCOE by roughly 5–6% relative to the base case.

- 80% CF can increase LCOE by roughly 6%.
- 70% CF can increase LCOE by roughly 20–22%, which would seriously weaken the investment case.

For IRR, a move from 85% to 70% capacity factor could lower returns by roughly 2–4 percentage points, depending on tariff level and debt structure. Conversely, operating above 85% strengthens cash flow quickly because geothermal has high fixed costs and low marginal generation cost. Below is a compact sensitivity analysis (**Table 11**) for the reported geothermal economics, using the baseline ranges and standard directional effects on project performance.

Table 11. Sensitivity analysis.

Scenario	Drilling Success rate	Wellfield Development Cost	Reservoir Temperature	Capacity Factor	LCOE (USD/kWh)	IRR (%)
Optimistic	90%	−10%	160 °C	90%	0.07–0.08	17–18
Base case	75–85%	Baseline	150–155 °C	85%	0.08–0.09	15–16
Conservative	60–70%	+10–20%	140–145 °C	70–80%	0.09–0.11	12–14

The sensitivity analysis shows that LCOE and IRR are most strongly influenced by drilling success rate and wellfield development cost, while reservoir temperature and capacity factor provide secondary but still significant effects; under optimistic assumptions, the LCOE may fall to 0.07–0.08 USD/kWh with IRR of 17–18%, whereas conservative assumptions may raise LCOE to 0.09–0.11 USD/kWh and reduce IRR to 12–14%. This means that drilling success rate and wellfield development cost directly affect the amount of productive capacity delivered per dollar invested. Reservoir temperature mainly shifts binary-cycle efficiency, so hotter reservoirs lower LCOE and improve IRR, while cooler reservoirs do the opposite. Capacity factor affects annual energy output almost linearly, so a drop from 85 % to 70 % can materially weaken project economics even if capital cost stays unchanged.

The geothermal data from studied sites demonstrate strong exploitation potential: temperature profiles confirm the accessibility of heat at shallow depths, the heat flow validates the presence of a magmatic source, and the energy potential indicates the possibility of producing several megawatts per site, with a reservoir lifespan exceeding 25 years without significant depletion. The probability of success remains high, with a manageable risk of one in four wells being dry, while costs benefit from economies of scale; the larger the plant, the lower the cost per kilowatt. Economically, the levelized cost of energy (LCOE) is approximately 9 US cents per kWh (0.089 $/kWh), which is well below Diesel (25 cents) and competitive with solar paired with batteries; the payback period is about 9 years to recover construction costs, an excellent timeline for an energy project, followed by 25 to 30 years of production. In summary, Meiganga represents a profitable and priority project for Cameroon, offering clean, local and stable energy that would reduce dependence on drought-vulnerable hydroelectric dams and imported diesel.

8. Conclusions

Cameroon's Cameroon Volcanic Line (CVL) represents Central Africa's premier geothermal opportunity, with 500–1,000 MWe recoverable resources across medium-enthalpy prospects demonstrating commercial viability through LCOE of 0.07–0.10 USD/kWh competitive with hydropower (0.07 USD/kWh) and superior to diesel (0.25 USD/kWh). Integrated geological, geochemical, and geophysical synthesis confirms gradients of 40–60 °C/km, heat flow anomalies of 155 mW/m^2, and reservoir temperatures of 145–162 °C at priority sites Meiganga, Tignère, and Ekondo-Titi, suitable for binary ORC power generation yielding 11.9% efficiency and cascade direct-use applications (fish drying, agro-processing) generating 7.5 MUSD/year revenue potential.

Despite promising fundamentals, development faces three critical barriers: exploration data scarcity (<15 wells drilled), absence of geothermal legislation, and technical capacity limitations, addressable through the proposed 2028–2035 roadmap prioritizing Meiganga 5 MW pilot ($45 M CAPEX), Tignère geophysics ($3.5 M), and legislative reforms (0% import duties, 10-year tax holiday). Phased implementation scales to 200 MWe operational capacity by 2035, delivering 1.7 TWh/year baseload power (capacity factor > 85%), displacing 5 $MtCO_2$ annually, and creating 2,000+ direct jobs whilst enabling industrial growth in aluminium smelting (1,200 MW potential) and cement production. This strategic deployment positions Cameroon as Central Africa's geothermal leader, contributing 10–15% to the 2035 National Energy Strategy's 25% renewables target amidst chronic 2.2 GW peak deficits and 15–40% load shedding. Successful execution requires financial mobilization and multi-stakeholder coordination to transform CVL's theoretical potential into sustainable energy reality.

8.1. Recommendations

1. Immediate/short term action (2028): Launch Meiganga 5 MW pilot ($45 M CAPEX, Q4 2028 commissioning) funded via AfDB SEFA grants covering 100% exploration phase, achieving LCOE 0.09 USD/kWh and demonstrating bankability.
2. Geophysical De-Risking: Allocate $3.5M for Tignère MT/ERT surveys and 2 slim-holes (Q1 2028 tender), targeting >42 °C/km gradients to unlock 20 MW Phase 2 by 2030.
3. Legislative Framework: Enact geothermal law by Q3 2028 via presidential decree, including 0% import duties on drilling rigs, 10-year corporate tax holiday, and <12-month permitting to attract EPC contractors.
4. Financing Mobilization: Secure $815 M for 2028–2035 roadmap through 60% AfDB debt (6%, 20-yr), 30% GET FiT equity auctions, and $15/t carbon credits, ensuring DSCR > 1.68× at $0.10/kWh PPA.
5. Capacity Building: Establish National Geothermal Training Centre, targeting 200 technicians by 2030 via IRENA/GETF partnerships.

8.2. Future Outlooks

The main limitations remain data scarcity, drilling uncertainty, incomplete reservoir characterization, lack of geothermal legislation, and technical capacity limitations. For this reason, future work should prioritize deep exploration wells, improved geophysical coverage, reservoir modeling, and full sensitivity analysis of project economics. In addition, Cameroon would benefit from geothermal legislation, institutional capacity building, and pilot-financing mechanisms that can reduce early-stage risk.

Future development should follow a phased pathway: reconnaissance studies, slim-hole confirmation, pilot production, then scale-up where warranted. This strategy is technically safer and financially more realistic than immediate large-scale deployment. If implemented carefully, geothermal energy could become an important component of Cameroon's long-term low-carbon energy mix.

Author Contributions

Conceptualization: E.M., F.N. and I.M.M.; Methodology: E.M., F.N., and D.N.; Software: E.M. and B.K.I.; Formal analysis: E.M., B.K.I. and I.M.M.; Investigation: E.M., F.N. and I.M.M.; Writing—Original Draft: E.M., F.N. and B.K.I.; Writing—Review and Editing: E.M., B.K.I. and I.M.M.; Validation: E.M., I.M.M. and D.N.; Data curation: F.N. and I.M.M.; Visualization: E.M., B.K.I. and I.M.M.; Project administration: I.M.M. and D.N.; Supervision: D.N. All authors have read and agreed to the published version of the manuscript.

Funding

This research received no external funding.

Institutional Review Board Statement

Not applicable.

Informed Consent Statement

Not applicable.

Data Availability Statement

Data is available upon reasonable request.

Conflicts of Interest

The authors declare that there is no conflict of interest regarding the publication of this paper.

AI Use Statement

AI was employed solely for language editing and proofreading support. During the preparation of this manuscript, the authors used Deepl solely for language refinement. No AI tools were used for data analysis, interpretation, or generation of scientific content. All outputs were critically reviewed and edited by the authors. The authors take full responsibility for the integrity and accuracy of the work.

Abbreviation

Terms	**Meaning**	**Units**
2-D	Two-Dimensional	—
3-D	Three-Dimensional	—
ARSEL	Electricity Sector Regulatory Agency of Cameroon	—
BHT	Bottom-Hole Temperature	°C
CAPEX	Capital Expenditure	USD
CEMAC	Economic and Monetary Community of Central Africa	—
CF	Cash-flow	USD
CHL	Cameroon Hot Line	—
CO_2	Carbon dioxide	—
CPD	Curie Point Depth	km
CVL	Cameroon Volcanic Line	km
Darcy	Darcy velocity law	m/s
DSCR	Debt Service Coverage Ratio	—
EPC	Engineering, Procurement, Construction	USD
ERT	Electrical Resistivity Tomography	Ω·m, m
GSHP	Ground-Source Heat Pump	—
Hrad	Radiogenic heat production	$\mu W/m^3$
IRR	Internal Rate of Return	%
LCOE	Levelized Cost of Electricity	USD/kWh
MT	Magnetotelluric	Ω·m
MWe	Megawatt electrical	MW
MWt	Megawatt thermal	MW
NPV	Net Present Value	USD
ORC	Organic Rankine Cycle	—
PPA	Power Purchase Agreement	USD/kWh
SCC	Specific Capital Cost	USD/kW
SMOW	Standard Mean Ocean Water	‰
WACC	Weighted Average Cost of Capital	%
Symbols	**Meaning**	**Units**
A	Coefficient in heat-flow relation	varies
CF_t	Net cash flow in year t	USD
c_r	Rock specific heat capacity	J/(kg·K)
c_p	Specific heat capacity	J/(kg·K)
E_t	Energy generated in year t	kWh
E_{el}	Electrical energy	kWh
E_{rec}	Recoverable energy	J, PJ
E_{therm}	Thermal energy in reservoir	J, PJ
ε	Recuperator effectiveness	—
η_{cycle}	Cycle efficiency	%
η_{plant}	Plant efficiency	%
f_{rec}	Recovery factor	—
G	Geothermal gradient	°C/km
h	Specific enthalpy	kJ/kg
$H(z)$	Internal/radiogenic heat production	W/m^3
I_t	Investment expenditure in year t	USD
k, λ	Thermal conductivity	W/(m·K)
k_{rl},k_{rg}	Relative permeabilities	—
k	Permeability	m^2
K	Permeability tensor	m^2
m_{wf}	Working-fluid mass flow rate	kg/s

m_{geo}	Geothermal-fluid mass flow rate	kg/s
NPV	Net present value	USD
P_{el}	Electrical power/potential	MW
P_{rated}	Rated electrical power	MW
P	Pressure	Pa
Q_z	Vertical heat flow	W/m^2
Q_{geo}	Geothermal heat input	W
Q_{out}	Useful heat delivered	W
q_l,q_g	Source/sink terms	depends
r	Discount rate	—
S_l,S_g	Phase saturations	—
T	Temperature	°C or K
T_c	Curie temperature	°C
T_{eq}	Equilibrium temperature	°C
$T_{geo,in}$,$T_{geo,out}$	Geothermal fluid inlet/outlet temperature	°C
T_0	Reference surface temperature	°C
T_r	Reservoir temperature	°C
t	Time/project lifetime	s, years
u_r	Rock internal energy	J/kg
V_r	Reservoir volume	m^3
v,v_l,v_g	Darcy velocity	m/s
W	Internal heat source	W
W_{net}	Net power output	W
W_{out}	Mechanical power output	W
Z_c	Curie point depth	km
Z_{h},Z_t	Depths to centroid and top of magnetic sources	km
ϕ	Porosity	—
ρ,ρ_r,ρ_l,ρ_g	Density	kg/m^3
μ,μ_l,μ_g	Dynamic viscosity	Pa·s
$\delta^{18}O$	Oxygen isotope ratio shift	‰
$\delta^{2}H$	Hydrogen isotope ratio shift	‰
$\delta^{13}C$-CO_2	Carbon isotope signature	‰

Units	**Meaning**	**Typical Use in the Manuscript**
m	Meter	Depth, thickness, well depth
km	Kilometer	Depth, distance, geothermal gradient denominator
m^2	Square meter	Area
m^3	Cubic meter	Reservoir volume
s	Second	Time
years	Year	Project lifetime, plant lifetime
°C	Degree Celsius	Temperature
K	Kelvin	Temperature in thermodynamics
°C/km	Degrees Celsius per kilometer	Geothermal gradient
W	Watt	Power, heat flow
W/m^2	Watts per square meter	Heat flow
W/m^3	Watts per cubic meter	Radiogenic heat production
W/(m·K)	Thermal conductivity unit	Conductivity k or λ
kg	Kilogram	Mass
kg/s	Kilograms per second	Mass flow rate
kg/m^3	Kilograms per cubic meter	Density
J	Joule	Energy
J/(kg·K)	Joule per kilogram per kelvin	Specific heat capacity
Pa	Pascal	Pressure
Pa·s	Pascal-second	Viscosity
Ω·m	Ohm-meter	Resistivity
mGal	Milligal	Gravity anomaly
mW/m^2	Milliwatt per square meter	Heat flow
$\mu W/m^3$	Microwatt per cubic meter	Radiogenic heat production
PJ	Petajoule	Large energy quantities
GWh	Gigawatt-hour	Electricity generation
MW	Megawatt	Electrical or thermal power

MWe	Megawatt electrical	Electric capacity
MWt	Megawatt thermal	Thermal capacity
USD	US dollars	Costs, CAPEX, revenue
USD/kWh	US dollars per kilowatt-hour	Electricity cost
USD/kW	US dollars per kilowatt	Specific capital cost
‰	Per mille	Isotope ratios
%	Percent	Efficiency, probability, shares
L/s	Liters per second	Spring discharge, flow rate
m.a.s.l.	Meters above sea level	Recharge elevation

References

1. ARSEL. *General Overview of the Energy Sector*; Autorité de Régulation du Secteur de l'Électricité: Yaoundé, Cameroon, 2023. (in French)
2. World Bank. *Scaling up Geothermal Energy in Developing Countries*; World Bank: Washington, DC, USA, 2023.
3. ENEO. *Annual Performance Report*; Energy of Cameroon: Douala, Cameroon, 2025. (in French)
4. IRENA. *Geothermal Direct-Use Opportunities in Africa*; International Renewable Energy Agency: Abu Dhabi, United Arab Emirates, 2025.
5. DiPippo, R. *Geothermal Power Generation: Developments and Innovation*; Elsevier: Amsterdam, The Netherlands, 2016.
6. Ko, I.J.; Choe, T.G. Prediction of Groundwater Temperature Variation in Riverine Well for the Safe Operation of Groundwater Heat Pump (GWHP) System. *Clean Energy Technol.* **2025**, *1*, 41–57. [CrossRef]
7. Investir au Cameroun. Electricity: Scatec Finalizes Two New 25–30 MW Solar Projects in Cameroon with IFC Financial Support. Available online: https://www.investiraucameroun.com/energie/1412-20107-electricite-scatec-peaufine-deux-nouveaux-projets-de-25-a-30-mw-de-solaire-au-cameroun-avec-l-appui-financier-de-la-sfi (accessed on 3 July 2025). (in French)
8. Déruelle, B.; Ngounouno, I.; Demaiffe, D. The "Cameroon Hot Line" (CHL): A Unique Example of Active Alkaline Intraplate Structure in Both Oceanic and Continental Lithospheres. *C. R. Geosci.* **2007**, *339*, 589–600. [CrossRef]
9. Mathieu, L. Quantifying Hydrothermal Alteration: A Review of Methods. *Geosciences* **2018**, *8*, 245. [CrossRef]
10. Vishiti, A.; Armstrong, T.; Shemang, E.; et al. Hydrothermal Alteration of Basaltic Rocks at Eruptive Vents on Mount Cameroon Volcano, West Africa. *Int. J. Geosci.* **2018**, *9*, 513–527. [CrossRef]
11. Nyaban, C.E.; Ndougsa-Mbarga, T.; Bikoro-Bi-Alou, M.; et al. Multi-Scale Analysis and Modelling of Aeromagnetic Data over the Bétaré-Oya Area in Eastern Cameroon, for Structural Evidence Investigations. *Solid Earth* **2021**, *12*, 785–800. [CrossRef]
12. Meying, A.; Wassouo, B.W.E.; Gouet, D.; et al. Hydrogeophysical Investigation for Groundwater Resources from Electrical Resistivity Tomography and Self-Potential Data in the Méiganga Area, Adamawa, Cameroon. *Int. J. Geophys.* **2018**, *2018*, 2697585. [CrossRef]
13. Ntomb Biboum, E.O.; Lepatio Tchieg, S.A.; Fosso Téguia, M.E.E.; et al. Contribution of Gravity and Hydrogeological Implication to the Study of the Subsoil in the East Region (Cameroon). *J. Geosci. Geomatics* **2021**, *9*, 45–54. [CrossRef]
14. Gnamou, B.; Ilboudo, H.; Toé, W.; et al. Geochemical Mobility Associated to Gold and Base Metal Occurrences of Mangodara Sector, in Southern Burkina Faso, Banfora Greenstone Belts (West African Craton). *Open J. Geol.* **2023**, *13*, 1024–1053. [CrossRef]
15. Fournier, R.O. Chemical Geothermometers and Mixing Models for Geothermal Systems. *Geothermics* **1977**, *5*, 41–50. [CrossRef]
16. Adams, A.N.; Wiens, D.A.; Nyblade, A.A.; et al. Lithospheric Instability and the Source of the Cameroon Volcanic Line: Evidence from Rayleigh Wave Phase Velocity Tomography. *J. Geophys. Res. Solid Earth* **2015**, *120*, 1708–1727.
17. KenGen. *Olkaria Geothermal Field: Binary Cycle Operations Report*; Kenya Electricity Generating Company: Nairobi, Kenya, 2024.
18. Emekwi, P.L.; Mariita, N.O.; Kariuki, P.C. Structural Controls Analysis and Its Correlation with Geothermal Occurrence at Barrier Volcanic Complex (BVC), Turkana, Kenya. *Int. J. Geosci.* **2024**, *15*, 231–245. [CrossRef]
19. Mouzong, M.P.; Mfetoum, M.I.; Ngoh, K.S.; et al. Current Status, Future Prospects, and the Need for Geothermal Energy Exploration in Cameroon: Comprehensive Review. *Geofluids* **2023**, *2023*, 6168519. [CrossRef]
20. Elvis, B.W.W. Hydrogeophysical study of the Meiganga area (Adamawa, Cameroon) using a combination of geoelectrical methods (direct current and spontaneous potential) and satellite imagery. Available online: https://dicames.online/jspui/handle/20.500.12177/12752 (accessed on 30 June 2025). (in French)
21. Alsoudi, M.; Mukbel, M. Renewable Energy Resources in Yemen: Growth, Challenges, Potential Opportunities and Strategies. *J. Power Energy Eng.* **2025**, *13*, 27–39. [CrossRef]
22. Hu, F.; Ducea, M.N.; Chapman, J.B.; et al. High Geothermal Gradients Facilitating Lithium Mineralization: Insights from the Ke'eryin–Taiyanghe Plutons, Central China. *Earth Planet. Sci. Lett.* **2025**, *672*, 119693. [CrossRef]
23. Hadzari, N.H.M.; Nasir, F.M.; Rahim, S.L. Design Optimization of an Organic Rankine Cycle with Different Operating Parameters for Heat Recovery from Industrial Kiln. In *Progress in Engineering Technology VI*; Razak, T.A.A., Ismail, A.K., Öchsner,

A., Eds.; Springer: Cham, Switzerland, 2025; pp. 81–88. [CrossRef]
24. Nemzouea, P.N.N.; Keutchafo, N.A.K.; Tchouankoue, J.P. Geothermal Development in Cameroon. *Eng. Therm.* **2020**, *19*, 32–41.
25. Ngako, V.; Njonfang, E.; Aka, F.T.; et al. The North-South Paleozoic to Quaternary Trend of Alkaline Magmatism from Niger-Nigeria to Cameroon: Complex Interaction between Hotspots and Precambrian Faults. *J. Afr. Earth Sci.* **2006**, *45*, 241–256.
26. Njonfang, E.; Ngako, V.; Kwekam, M.; et al. The Foumban-Bankim Calc-Alkaline Orthogneisses: Evidence of a Sheared Internal Zone of a Pan-African Active Margin. *C. R. Geosci.* **2006**, *338*, 606–616. (in French) [CrossRef]
27. Ebinger, C.J.; Sleep, N.H. Cenozoic Magmatism throughout East Africa Resulting from Impact of a Single Plume. *Nature* **1998**, *395*, 788–791. [CrossRef]
28. Seghedi, I.; Downes, H.; Szakacs, A.; et al. Neogene Quaternary Magmatism and Geodynamics in the Carpathian-Pannonian Region: A Synthesis. *Lithos* **2004**, *72*, 117–146. [CrossRef]
29. Mantovani, E.; Viti, M.; Babbucci, D.; et al. Generation of Back-Arc Basins as Side Effect of Shortening Processes: Examples from the Central Mediterranean. *Int. J. Geosci.* **2014**, *5*, 1062–1079. [CrossRef]
30. Fitton, J.G.; Dunlop, H.M. The Cameroon Line, West Africa, and Its Bearing on the Origin of Oceanic and Continental Alkali Basalt. *Earth Planet. Sci. Lett.* **1985**, *72*, 23–38. [CrossRef]
31. Tchuimegnie Ngongang, N.B.; Wagsong, M.P.N.; Owono, F.M.; et al. Mineralogy and Magmatic Processes of Cenozoic Intraplate Alkaline Volcanic Rocks of Bafang and Its Environs (Cameroon Volcanic Line, West Africa). *Open J. Geol.* **2021**, *11*, 210–238. [CrossRef]
32. Marzoli, A.; Renne, P.R.; Piccirillo, E.M.; et al. Silicic Magmas from the Continental Cameroon Volcanic Line (Oku, Bambouto and Ngaoundere): 40Ar-39Ar Dates, Petrology, Sr-Nd-O Isotopes and Their Petrogenetic Significance. *Contrib. Mineral. Petrol.* **1999**, *135*, 133–150
33. Meyers, J.B.; Rosendahl, B.R.; Harrison, C.G.A.; et al. Deep-Imaging Seismic and Gravity Results from the Offshore Cameroon Volcanic Line, and Speculation of African Hotlines. *Tectonophysics* **1998**, *284*, 31–63
34. Lima, E.; Tokita, H.; Hatanaka, H. Reservoir Engineering in Geothermal Fields. In *Encyclopedia of Sustainability Science and Technology*; Meyers, R., Ed.; Springer: New York, NY, USA, 2017. [CrossRef]
35. White, M.; Vasyliv, Y.; Beckers, K.; et al. Numerical Investigation of Closed-Loop Geothermal Systems in Deep Geothermal Reservoirs. *Geothermics* **2024**, *116*, 102852. [CrossRef]
36. Njonfang, E.; Ngako, V.; Moreau, C.; et al. Restraining Bends in High Temperature Shear Zones: The Central Cameroon Shear Zone, Central Africa. *J. Afr. Earth Sci.* **2008**, *52*, 9–20. [CrossRef]
37. Kahraman, M.; Cornwell, D.G.; Thompson, D.A.; et al. Crustal-Scale Shear Zones and Heterogeneous Structure beneath the North Anatolian Fault Zone, Turkey, Revealed by a High-Density Seismometer Array. *Earth Planet. Sci. Lett.* **2015**, *430*, 129–139. [CrossRef]
38. Aydin, U.; Pamuk, E.; Ozer, C. Investigation of Soil Dynamic Characteristics at Seismic Stations Using H/V Spectral Ratio Method in Marmara Region, Turkey. *Nat. Hazards* **2021**, *110*, 587–606. [CrossRef]
39. Ibrahim, M.W. Geothermal Gradient Anomalies of Hydrocarbon Entrapment, UKCS Quadrants 35–54. In Proceedings of the European Petroleum Computer Conference, Aberdeen, UK, 15–17 March 1994; pp. 85–96.
40. Mao, X.; Li, K. Main Controlling Factors of Regional High Geothermal Anomaly. In Proceedings of the 43rd Workshop on Geothermal Reservoir Engineering, Stanford University, Stanford, CA, USA, 12–14 February 2018.
41. Nono, A.; Déruelle, B.; Demaiffe, D.; et al. Tchabal Nganha Volcano in Adamawa (Cameroon): Petrology of a Continental Alkaline Lava Series. *J. Volcanol. Geotherm. Res.* **1994**, *60*, 147–178
42. Shariatipour, S.M.; Pickup, G.E.; Mackay, E.J. The Effect of Aquifer/Caprock Interface on Geological Storage of CO_2. *Energy Procedia* **2014**, *63*, 5544–5555. [CrossRef]
43. Ziem à Bidias, L.A.; Moundi, A.; Takodjou Wambo, J.D. Transitional Basalts and Erruptive Dynamisms Around Nkoumelap Locality (West of the Bamoun Plateau, Cameroon Volcanic Line): Petrography and Volcanic Risks' Evaluation. *J. Geosci. Geomatics* **2017**, *5*, 65–77
44. Njeudjang, K.; Abate Essi, J.M.; Domra Kana, J.; et al. Gravity Investigation of the Cameroon Volcanic Line in Adamawa Region: Geothermal Features and Structural Control. *J. Afr. Earth Sci.* **2020**, *165*, 103809. [CrossRef]
45. Eyike, A.; Nyam, F.; Basseka, C. Topography of the Moho Undulation in Cameroon from Gravity Data: Preliminary Insights into the Origin, the Age and the Structure of the Crust and the Upper Mantle across Cameroon and Adjacent Areas. *Open J. Geol.* **2018**, *8*, 65–85. [CrossRef]
46. Kendon, E.J.; Stratton, R.A.; Tucker, S. Enhanced Future Changes in Wet and Dry Extremes over Africa at Convection-Permitting Scale. *Nat. Commun.* **2019**, *10*, 1794. [CrossRef]
47. Joel, P.K.; Louise-Clotilde, O.A.M.; Evariste, N.; et al. Identification of Geothermal Reservoirs in South Cameroon from a Combined Landsat 8 and AMT Data. *Int. J. Geophys.* **2022**, *2022*, 1324766. [CrossRef]
48. Ndongmo, G.; Koumetio, F.; Ngapgue, F.; et al. Characterization of Near Surface Intrusions in South-West Cameroon Zone Using Gravity Data: Mining and Geothermal Implications. *J. Geosci. Environ. Prot.* **2023**, *11*, 268–296. [CrossRef]
49. Ngoh, J.D.; Mbarga, T.N.; Mickus, K.; et al. Estimation of Curie Point Depth (CPD) across the Pan African Belt in Northern Cameroon from Aeromagnetic Data. *Open J. Earthq. Res.* **2020**, *9*, 217–239. [CrossRef]
50. Abdel Zaher, M.; El-Qady, G.; Elbarbary, S. Geothermal Potentiality of Egypt: Review and Updated Status. In *The Phanerozoic Geology and Natural Resources of Egypt*; Hamimi, Z., Khozyem, H., Adatte, T., et al., Eds.; Springer International Pub-

lishing: Cham, Switzerland, 2023; pp. 637–648. [CrossRef]
51. Abraham, E.; Okechukwu, P. Modeling Geothermal Energy Potential in the Ruwan-Zafi Hot Spring Region of Northeastern Nigeria Using High-Resolution Aeromagnetic Data. *Model. Earth Syst. Environ.* **2024**, *10*, 4361–4373. [CrossRef]
52. Michaut, C.; Jaupart, C.; Bell, D.R. Transient Geotherms in Archean Continental Lithosphere: New Constraints on Thickness and Heat Production of the Subcontinental Lithospheric Mantle. *J. Geophys. Res.* **2007**, *112*. [CrossRef]
53. Clauser, C.; Huenges, E. Thermal Conductivity of Rocks and Minerals. In *Rock Physics & Phase Relations: A Handbook of Physical Constants*; American Geophysical Union: Washington, DC, USA, 2013; pp. 105–126. [CrossRef]
54. Arola, T.; Okkonen, J.; Jokisalo, J. Groundwater Utilisation for Energy Production in the Nordic Environment: An Energy Simulation and Hydrogeological Modelling Approach. *J. Water Resour. Prot.* **2016**, *8*, 642–656. [CrossRef]
55. Tanaka, A.; Okubo, Y.; Matsubayashi, O. Curie Point Depth Based on Spectrum Analysis of the Magnetic Anomaly Data in East and Southeast Asia. *Tectonophysics* **1999**, *306*, 461–470. [CrossRef]
56. Langemeyer, S.M.; Lowman, J.P.; Tackley, P.J. Global Mantle Convection Models Produce Transform Offsets along Divergent Plate Boundaries. *Commun. Earth Environ.* **2021**, *2*, 69. [CrossRef]
57. Arnórsson, S.; Andrésdóttir, A. Processes Controlling the Distribution of Boron and Chlorine in Natural Waters in Iceland. *Geochim. Cosmochim. Acta* **1995**, *59*, 4125–4146. [CrossRef]
58. Giggenbach, W.F. Isotopic Shifts in Water from Geothermal and Hydrothermal Systems along Convergent Plate Boundaries and Their Origin. *Earth Planet. Sci. Lett.* **1992**, *113*, 495–510. [CrossRef]
59. Sanjuan, B.; Asmundsson, R.; Millot, R.; et al. Use of Two New Na/Li Geothermometric Relationships for Geothermal Fluids in Volcanic Environments. In Proceedings of the Goldschmidt Conference 2012, Montréal, QC, Canada, 24–29 June 2012.
60. Hayashi, K. Oxygen Isotope Study of Silica Sinter from the Osorezan Geothermal Field, Northeast Japan. *Int. J. Geosci.* **2013**, *4*, 1438–1446. [CrossRef]
61. Jaupart, C.; Mareschal, J.-C. *Heat Generation and Transport in the Earth*; Cambridge University Press: Cambridge, UK, 2010.
62. Turcotte, D.L.; Schubert, G. *Geodynamics*; Cambridge University Press: Cambridge, UK, 2002. [CrossRef]
63. Loke, M.H. Topographic Modelling in Resistivity Imaging Inversion. In Proceedings of the 62nd EAGE Conference & Technical Exhibition, Glasgow, Scotland, 29 May–2 June 2000.
64. Hart, R.M.; Ikard, S.J.; Hays, P.D.; et al. *Effects of Climate and Land-Use Change on Thermal Springs Recharge—A System-Based Coupled Surface-Water and Groundwater-Flow Model for Hot Springs National Park, Arkansas*; U.S. Geological Survey: Reston, VA, USA, 2021. [CrossRef]
65. Eissa, R. Identification of Different Shallow Foundations Using 3-D Electrical Resistivity Modeling. *Iraqi Geol. J.* **2022**, *55*, 111–120
66. Constable, S.; Parker, R.L.; Constable, C. Occam's Inversion: A Practical Algorithm for Generating Smooth Models from Electromagnetic Sounding Data. *Geophysics* **1987**, *52*, 289–300. [CrossRef]
67. Martínez-Garzón, P.; Meier, M.-A.; Collettini, C.; et al. Stress Heterogeneities Governed by Fault Structure and Stress Transfer: The 2016–2017 Central Italy Seismic Sequence. *J. Geophys. Res. Solid Earth* **2025**, *130*, e2024JB029763. [CrossRef]
68. Gideon, Y.B. Petrography and Geochemical Characterization of Basement Rocks within Okene Metropolis, North Central Nigeria. *Int. J. Geol. Earth Environ. Sci.* **2019**, *9*, 36–48
69. Adamu, L.M.; Umaru, A.O.; Aliyu, A.E.; et al. Geology, Geochemistry and Petrogenetic Studies of the Precambrian Basement Rocks around Jimgbe, Northcentral Nigeria. *J. Min. Geol.* **2021**, *57*, 229–240
70. Ndikum, E.N.; Koumetio, F.; Kenfack, V.J.; et al. Gravity Study of the Douala Sub-Basin (Cameroon) Using Euler 3-D Deconvolution, Source Edge Detection (SED) and Special Function Analysis. *SN Appl. Sci.* **2019**, *1*, 1200. [CrossRef]
71. Kamgang Chendjou, L.C.; Kenfack, J.V.; Tcheumenak Kouémo, J.; et al. Interpretation of Geological and Gravity Data from the Bamiléké Plateau (West-Cameroon): Implication for the Understanding of Its Underground Lithotectonic Geometry. *J. Geosci. Environ. Prot.* **2024**, *12*, 283–314. [CrossRef]
72. Elvis, B.W.W. Hydro-Geophysical Study of the Meiganga Zone (Adamaoua, Cameroon) by Combining Geo-Electrical Methods (Coutrant and Spontaneous Potential) and Satellite Imagery. PhD Thesis, Université de Yaoundé 1, Yaoundé, Cameroon, 2024.
73. O'Sullivan, M.J.; Pruess, K.; Lippmann, M.J. State of the Art of Geothermal Reservoir Simulation. *Geothermics* **2001**, *30*, 395–429
74. Xu, W.; Xie, X.; Yi, S.; et al. Evaluation of Hot Dry Rock Reservoir Stimulation Based on Microseismic Monitoring Method: A Case Study of the Northern Jiangsu Basin. *Front. Earth Sci.* **2025**, *13*, 1688302. [CrossRef]
75. Dagdas, A.; Akkoyunlu, M.T.; Basaran, T. Performance Analysis of Supercritical Binary Geothermal Power. *Adv. Mech. Eng.* **2014**, *7*, 326839
76. Lund, J.W. Geothermal Energy Utilization. In *Renewable Energy Systems*; Kaltschmitt, M., Themelis, N.J., Bronicki, L.Y., et al., Eds.; Springer: New York, NY, USA, 2013. [CrossRef]
77. Al-Zyoud, S. Geothermal Energy Utilization in Jordanian Deserts. *Int. J. Geosci.* **2019**, *10*, 906–918. [CrossRef]
78. Adepoju-Bello, A.A.; Ojomolade, O.O.; Ayoola, G.A.; et al. Quantitative Analysis of Some Toxic Metals in Domestic Water Obtained from Lagos Metropolis. *Niger. J. Pharm.* **2009**, *42*, 57–60
79. Akoachere II, R.A.; Eyong, T.A.; Ngassam, M.-C.P.; et al. Evaluation of Trace Metals in Groundwater of Ekondo-Titi and Environs, Onshore Rio Del Rey, Cameroun. *Open Access Libr. J.* **2019**, *6*, e5791. [CrossRef]
80. Mono, J.A.; Bouba, A.; Owono Amougou, O.U.I.; et al. Analysis of Aeromagnetic Data for Enhancing Geologic Features Using

Filtering Techniques over the Congo Craton–Pan-African Belt Contact, Centre-East Cameroon. *Int. J. Geophys.* **2024**, *2024*, 4767612. [CrossRef]
81. Bear, J. *Dynamics of Fluids in Porous Media*; Dover Publications: New York, NY, USA, 1988.
82. Gudmundsson, J.S. Two-Phase Flow in Geothermal Wells. In *Geothermal Reservoir Engineering*; Okandan, E., Ed.; Springer: Dordrecht, The Netherlands, 1988. [CrossRef]
83. Pud, D.; Treister, R.; Eisenberg, E. Sub-Grouping Healthy Subjects' Sensitivity to Pain and Its Relationship to Personality Traits: Results of a Cluster Analysis. *Am. J. Appl. Math.* **2014**, *5*, 1705–1712. [CrossRef]
84. Pratama, H.B.; Saptadji, N.M. Study of Production-Injection Strategies for Sustainable Production in Geothermal Reservoir Two-Phase by Numerical Simulation. *Indones. J. Geosci.* **2020**, *8*, 25–38
85. Pruess, K.; Oldenburg, C.M.; Moridis, G. *TOUGH2 User's Guide, Version 2*; Lawrence Berkeley National Laboratory (LBNL): Berkeley, CA, USA, 1999. [CrossRef]
86. Meacci, L. Modeling a Geothermal Field: A Not-Trivial Starter Kit. *Open Access Libr. J.* **2020**, *7*, e6836. [CrossRef]
87. Muffler, P.; Cataldi, R. Methods for Regional Assessment of Geothermal Resources. *Geothermics* **1978**, *7*, 53–89. [CrossRef]
88. Vieira, F.; Hamza, V. Advances in Assessment of Geothermal Resources of South America. *Nat. Resour.* **2014**, *5*, 897–913. [CrossRef]
89. Atrens, A.; Gurgenci, H.; Rudolph, V. CO_2 Thermosiphon for Competitive Geothermal Power Generation. *Energy Fuels* **2009**, *23*, 553–557.
90. Al-Fakih, A.; Li, K. Study of Geothermal Energy Resources of Yemen for Electric Power Generation. In Proceedings of the GRC's 42nd Annual Meeting & Expo, Reno, NV, USA, 14–17 October 2018.
91. Sanyal, S.K. Classification of Geothermal Systems—A Possible Scheme. In Proceedings of the 30th Workshop on Geothermal Reservoir Engineering, Stanford, CA, USA, 31 January–2 February 2005.
92. Khodayar, M.; Björnsson, S. Conventional Geothermal Systems and Unconventional Geothermal Developments: An Overview. *Open J. Geol.* **2024**, *14*, 196–246. [CrossRef]
93. Kolie, B.; Elshkaki, A.; Sunahara, G. The Impact of the Energy Transition and Sustainable Development Goals on Mineral Resource Availability in Africa. *Smart Grid Renew. Energy* **2024**, *15*, 149–185. [CrossRef]
94. Tester, J.; Blackwell, D.; Petty, S.; et al. The Future of Geothermal Energy: An Assessment of the Energy Supply Potential of Engineered Geothermal Systems (EGS) for the United States. In Proceedings of the Thirty-Second Workshop on Geothermal Reservoir Engineering, Stanford, CA, USA, 22–24 January 2007.
95. Terry-Short, L.A.; Owens, R.G.; Slade, P.D.; et al. Positive and Negative Perfectionism. *Pers. Individ. Dif.* **1995**, *18*, 663–668. [CrossRef]
96. IEA. The Future of Geothermal Energy. Available online: https://www.iea.org/reports/the-future-of-geothermal-energy (accessed on 14 June 2025).
97. Dobson, P.; Asanuma, H.; Huenges, E.; et al. Supercritical Geothermal Systems—A Review of Past Studies and Ongoing Research Activities. In Proceedings of the 41st Workshop on Geothermal Reservoir Engineering, Stanford, CA, USA, 13–15 February 2017.
98. Rodriquez, K.; Intawong, A.; Hodgson, N.; et al. *Fractured Basement—An Overlooked Play Type with Significant Potential from a Global Seismic Database*; European Association of Geoscientists & Engineers: Bunnik, The Netherlands, 2017. [CrossRef]